Driving and Regulation of Macroscopic Motile Functions in Artificial and Living Systems by Molecular Photoswitches

光分子スイッチによる人工系および生体系での巨視的運動機能の駆動と制御

A Thesis

Submitted for the Degree of

Doctor of Life Science

By

Noushaba Nusrat Mafy

Laboratory of Smart Molecules

Transdisciplinary Life Science Course

Graduate School of Life Science,

Hokkaido University

September 2019

Declaration

I hereby declare that the matter embodied in this thesis entitled "**Driving and Regulation of Macroscopic Motile Functions in Artificial and Living Systems by Molecular Photoswitches**" is the result of investigations carried out by me under the supervision of ***Prof. Nobuyuki Tamaoki*** at the Laboratory of Smart molecules, Transdisciplinary Life Science Course, Graduate School of Life Science, Hokkaido University, Japan and it has not been submitted elsewhere for the award of any degree or diploma.

In keeping with the general practice of reporting scientific observations, due acknowledgement has been made whenever the work described has been based on the findings of the other investigators. Any omission that might have occurred by oversight or error of judgments is regretted.

Noushaba Nusrat Mafy

Certificate

I hereby certify that the work described in this thesis entitle "**Driving and Regulation of Macroscopic Motile Functions in Artificial and Living Systems by Molecular Photoswitches**" has been carried out by ***Noushaba Nusrat Mafy***, under my supervision at the Laboratory of Smart Molecules, Transdisciplinary Life Science Course, Graduate School of Life Science, Hokkaido University, Japan

Prof. Nobuyuki Tamaoki

(Research Supervisor)

Table of Contents

Chapter 1

General Introduction

Nature is overflowing with the diversity of life, which is surrounded by plants, animals, insects and so on. Life on the earth is composed of microscopic cells, which are themselves composed of nanoscale molecules. Where, microscopically cells are using nanoscale molecules to perform several motile functions, including transport of metabolites across cell membranes, signaling of nerve impulses, transport of chromosomes during cell division, generating force etc.[1] By using these cellular events, macroscopically plants are growing, animals are moving and doing work, insects are crawling or climbing etc. After examining these microscopic and macroscopic activities in living organisms, I can claim movement is one of the most indispensable parts from microscopic to macroscopic scale in the living system. All the macroscopic movements and other functions in living organisms or artificial systems are governed by these nanoscale molecules.[2] It is very inspiring to realize the amplification of these molecular events to the macroscopic movements. I used two systems to amplify the molecular level event to macroscopic scale. One was artificial cholesteric liquid crystalline system, where macroscopic rotational work was done by amplifying the molecular motion. Another one was living cellular system, where small molecule was used to control cell division by regulating the movement of chromosomes.

I introduced photoswitchable azobenzene based molecules in both systems because these molecules can switch between two isomeric forms in a reversible fashion by light. Light induced switching or photoswitching is most appealing approach because light can be considered as most advantageous non-invasive stimuli for both artificial and living systems which offers a very high spatial and temporal resolution, allowing for true remote control.[3-5] Illuminating with a specific light, the azobenzene molecule undergoes an reversible isomerization, which involves a change in the geometry and charge of the molecule from the more stable, less polar *trans* isomer to

the less stable, more polar *cis* isomer, the former having a rod-like shape, while the latter a bent conformation.[6-8] These changes in the structure induces different affinity toward the protein or liquid crystals and consequences in the reversible reorganization of the molecular system, which finally induces macroscopic change in the movement.[9-11] In case of non-photoresponsive molecule, it is impossible to change the condition without further addition of another molecule.

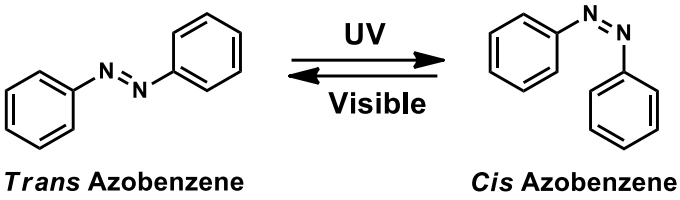

Figure1-1: Photoisomerization of azobenzene

Here, in both artificial and living cellular system, azobenzene based molecules efficiently amplified its isomerization information to control the macroscopic movements or mechanical functions and cellular events. Specifically, by amplifying the molecular motion artificial system generated continuous and unidirectional rotational work seen in engines in the real world and cellular system controlled its progression.

Following up to these results, the general goal of the work presented in this thesis is to amplify the concerted motions of nanosized molecules up to the macroscopic scale, by taking advantage of isomerization of azobenzene molecule.

In Chapter 2, I describe the molecular crankshaft effect converting piston-like molecular motion to continuous rotation of macro objects.

In Chapter 3, I explain optochemical regulation of Cenp-E and chromosome movement during mitosis cell division.

In chapter 4, conclusions of this thesis are mention.

References

(1) Goodsell, D. S. The Machinery of Life, 2nd edition, New York: Springer-Verlag, **2009.**

(2) Centore, R.; Causa, M. Translating Microscopic Molecular Motion into Macroscopic Body Motion: Reversible Self-Reshaping in the Solid State Transition of an Organic Crystal, *Cryst. Growth Des.* **2018,** *18*, 3535−3543.

(3) Russew, M.-M.; Hecht, S. Photoswitches: From Molecules to Materials, *Adv. Mater.,* **2010**, *22*, 3348–3360.

(4) Szymanski, W.; Beierle, J. M.; Kistemaker, H. A. V.; Velema, W. A.; Feringa, B. L. Reversible Photocontrol of Biological Systems by the Incorporation of Molecular Photoswitches. *Chem. Rev*., **2013**, *113*, 6114-6178

(5) Baroncini, M.; Groppi, J.; Corra, .; Silvi, S.; Credi, A. Light-Responsive (Supra)Molecular Architectures: Recent Advances. *Adv. Optical Mater.,* **2019**, DOI: 10.1002/adom.201900392.

(6) Hartley, G., The Cis-form of Azobenzene. *Nature,* **1937**, *140*, 281.

(7) Rau, H., Photoisomerization of Azobenzenes. Photochemistry and Photophysics, **1990**; Vol. *2*, pp 119-141.

(8) Mahimwalla, Z.; Yager, K. G.; Mamiya, J.-I.; Shishido, A.; Priimagi, A.; Barrett, C. J., Azobenzene Photomechanics: Prospects and Potential Applications. *Polym. Bull.,* **2012**, *69*, 967-1006.

(9) Beharry, A. A.; Woolley, G. A. Azobenzene Photoswitches for Biomolecules. *Chem. Soc. Rev.*, **2011**, *40*, 4422–4437.

(10) Tamaoki, N. Molecular Machines Based on Liquid Crystal, *Handbook of Liquid Crystals*, **2014**, *8*, 865-877.

(11) Tamaoki, N. Light-Driven Molecular Machine, *Functional Materials*, **2007**, *27*, 50-56.

Chapter 2

Optochemical Regulation of Cenp-E and Chromosome Movement During Mitosis Cell Division

2.1. Introduction

Mitosis cell division in eukaryotic cells generates two or more daughter cells from a parent cell through the equal distribution of their genetic information.[1] During this important process, chromosomes containing DNA are accurately replicated and dynamically transported. This dramatic movements of chromosomes, especially during metaphase, are regulated by motor proteins, which are the bio-transducers of chemical energy of ATP into mechanical motion. During metaphase, polar oriented laterally attached chromosomes are transported to equator along spindle microtubule and aligned at the metaphase plate (congression). Successful chromosome congression depends on the kinetochore-microtubule (MT) attachment, MT dynamics and force generation by biomotors.[2,3] There is a several methods to regulate the chromosome congression by controlling the function of biomotors. Ribonucleic acid interference (RNAi) mediated depletion of specific protein,[4] laser microsurgery,[5] antibody injection[6] and chemical inhibitor[7] are well known approach to control the function of proteins.

Two large families of molecular motors, kinesins and dynein, drive transportation of chromosomes along MT filaments. Kinesin 7 or centromere-associated protein E (Cenp-E)[8] transports the chromosomes to positive end of the spindle MT by hydrolysis of the ATP.[9,10] After complete alignment of chromosomes at metaphase plate, motor activity of Cenp-E is required or not still a controversial issue.[11,12] When the expression of Cenp-E is suppressed, or it's activity is inhibited, some chromosomes are failed to align at metaphase plate and retain to the spindle poles (miscongression), leading to mitotic arrest. In presence of misalinged chromosomes, kinetochore activate the spindle assembly checkpoint (SAC) proteins which turn off the cell cycle progression.[13] SAC monitor the attachment of

chromosomes to microtubule and proper alignment at the metaphase plate. After complete congression of chromosomes, SAC proteins are released from kinetochore and allow cell cycle progression.

To control the cell division by tuning the function of proteins and reveal the controversial function, such experimental tools are essential, which can reversibly manipulate the activity of proteins with spatiotemporal precision and molecular specificity. Optochemical tool will be most potential approach to get both reversible control and molecular specificity by using light. Borowiak *et al*. developed an optochemical tool, which can be switched ON and OFF by visible light and control the dynamics of MT and mitosis cell division in living cells.[14] Recently developed an optogenetic tool can control the kinetochore function of chromosomes with spatiotemporal precision.[15] This tool specially manipulates the checkpoint signaling and molecular motor activity in cells by recruiting the proteins to and release them from the kinetochore using light irradiation. But this system is irreversible and genetic modification is necessary for introducing their tool. By existing methods, it is impossible to achieve spatiotemporal control over the activity of motor proteins and cell division.

Kinetochore motor protein Cenp-E has achieved much attention as a potential target to control the cell division, because it's motor activity is essential for chromosome congression. Different approaches such as microinjection of antibody directed against Cenp-E,[11] siRNA mediated depletion of Cenp-E[13,16] and Cenp-E specific chemical inhibitors[7] has been used to regulate it's motor activity. Small molecule inhibitor is potential to use as therapeutic drug, but non-specific target and lack of spatiotemporal control limit it's use. There is a several small molecule Cenp-E inhibitors; GSK923295,[17] Syntelin,[18] PF-2771[19] and Cmpd-A[20] to stop cell cycle

progression. Using all these established small molecule inhibitors and other methods, it is impossible to control the activity of Cenp-E reversibly in living cells with spatiotemporal precision and explore the unrevealed function of Cenp-E during the mitosis cell division.

Our interest is on the development of an optochemical tool, by which activity of Cenp-E can be switched to ON and OFF manner using different wavelength of light. Herein, I developed the azobenzene-tethered reversibly photocontrollable Cenp-E inhibitor based on GSK923295 structure. Azobenzene derivatives have been widely accepted as photoswitches because of their notable changes in geometry upon isomerization, high quantum yields and fast photoisomerization rates.[21] I developed four photoswitchable inhibitors. Among them only inhibitor **4** showed the efficient photoisomerization and significant change of inhibition behavior under two isomer state in both isolated and living cell. Inhibitor **4** can control the movement of chromosomes for several cycles with spatiotemporal precision using UV and visible light irradiation. To introduce this inhibitor in cellular system, it is not necessary to do any genetic modification. This optochemical tool established a new platform to control the motor activity of Cenp-E as well as chromosome movement and reveal the functions of Cenp-E.

2.2 Results

2.2.1. Design of Photoswitchable Inhibitors

GSK923295 is first highly specific, potent and allosteric inhibitor of Cenp-E motor domain, which targets the ATPase activity of Cenp-E and has significant growth inhibitory effect in 237 panels of cancer cell lines *in vitro*.[17] The design of photoswitchable inhibitors for Cenp-E was inspired by the core structure of

GSK923295 (Figure 2-1). Already reported a great variety of structures based on the GSK923295 showed significant change in inhibition activity with different aryl moieties in different positions and different lengths of side chain.[22] Inspiring from this structural relationship with the inhibition of Cenp-E, I designed series of photoswitchable inhibitors, where photoswitchable azo moiety is tethered with phenyl group in *ortho*, *meta* and *para* positions (Inhibitor **1**, **3**, **2**) and 2,3,5-trimethyl pyrazole group at *para* position (Inhibitor **4**) by replacing the phenylimidazopyridinyl moiety and reduced the chain length in side chain of GSK923295 (Figure 2-1). All photoswitchable inhibitors in this study were prepared according to the detail synthetic procedure and confirmed by ^{1}H NMR, ^{13}C NMR and HR-MS are described in section 2.5.10.

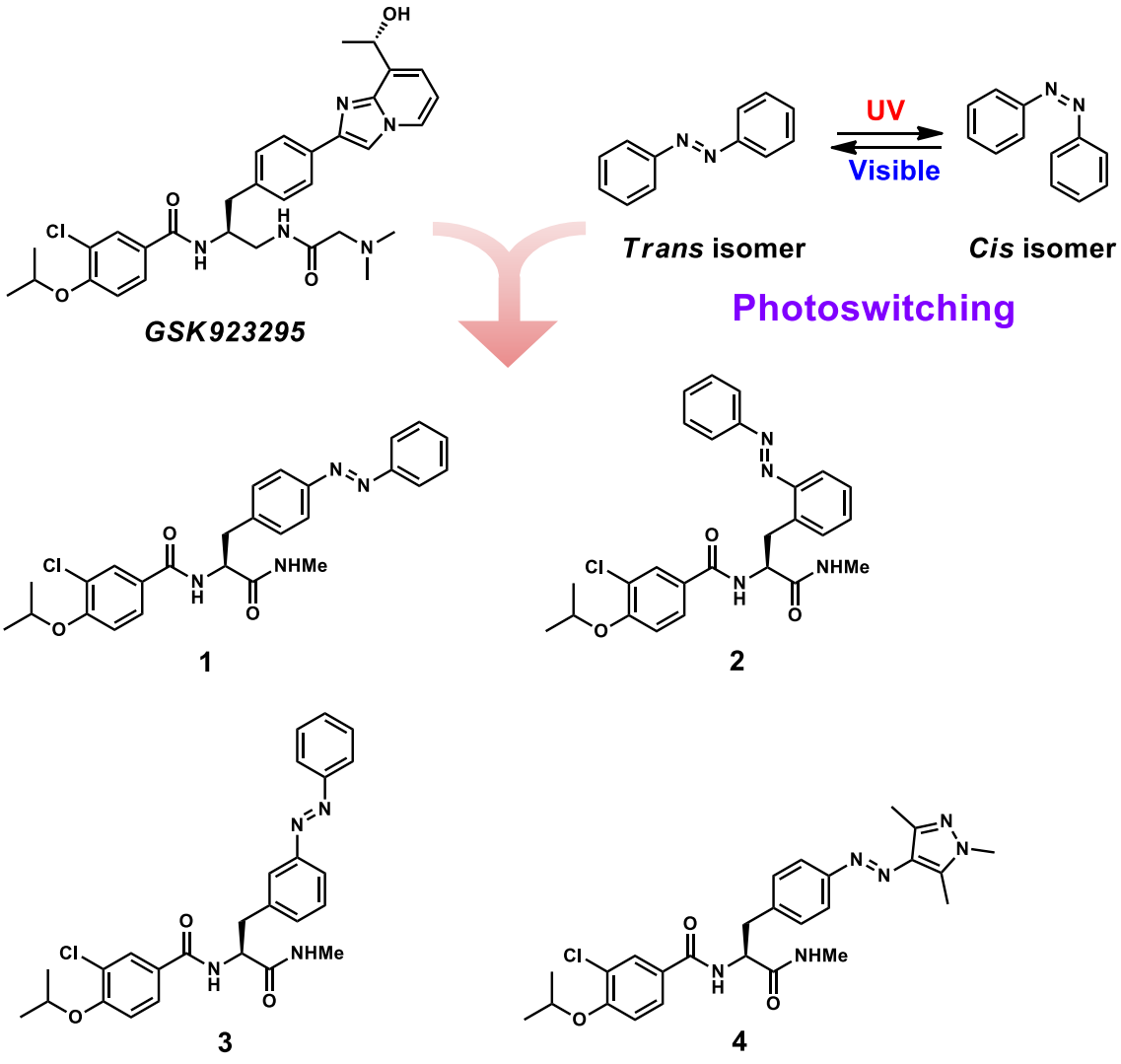

Figure 2-1. Structure of GSK923295 and designed azo-tethered photoswitchable Cenp-E inhibitors: **1.** *Ortho* **2.** *Para* **3.** *Meta* position of phenyl moiety **4.** *Para* position of 2,3,5-trimethyl pyrazole moiety.

2.2.2. Photophysical Properties of Inhibitors

The indispensable requirements to use the photoswitchable inhibitor are efficient and quick reversible photoisomerization between two different configurations with a relatively high degree of photoconversion (*trans* / *cis* ratio) at different wavelength of light and long-lived isomers. Azobenzene derivatives are privileged to use as bioactive compounds due to their fast and efficient photoisomerization and notable change in geometry and polarity between two isomers.[20] Initially thermally stable linear *trans* isomers are isomerized to bent shape, more polar *cis* isomers under UV light irradiation and reversely isomerized to *trans* by visible light irradiation (Figure 2-2a). Photophysical properties of all compounds were studied by UV-visible absorption spectroscopy and reverse phase high-performance liquid chromatography (RP-HPLC). UV-visible absorption spectra of inhibitor **1**-**4** are shown in Figure 2-2b-e. Under 365 nm light irradiation, *trans* isomers converted to *cis* isomers and reached to the *cis* rich state (UV photostationary state, PSS_{365nm}) and absorption around 330 nm for π–π* *trans*ition decreased, simultaneously absorption for n–π* *trans*ition around 450 nm increased. Reverse isomerization (*cis* to *trans*) occurs under 510 nm light irradiation and reached to *trans* rich state (visible photosationary state, PSS_{510nm}), consequently absorption for π–π* band increased and n–π* band decreased. All the compounds were efficiently and reversibly photoisomerized for many cycles without any fatigue (inset of Figure 2-2b to e). To evaluate the rate of thermal *cis-trans* relaxation, half-life of *cis* isomers for all compounds were determined at 37 °C (Figure 2-3a,b). For all photoswitchable inhibitors, half-life at 37 °C is >1 d, showing that the

cis isomer is relatively stable (Table2-1). Isomer ratio of all compounds at before irradiation (BI), PSS_{365nm}, PSS_{436nm} and PSS_{510nm} state were measured by RP-HPLC (Figure 2-3c and Table2-1).

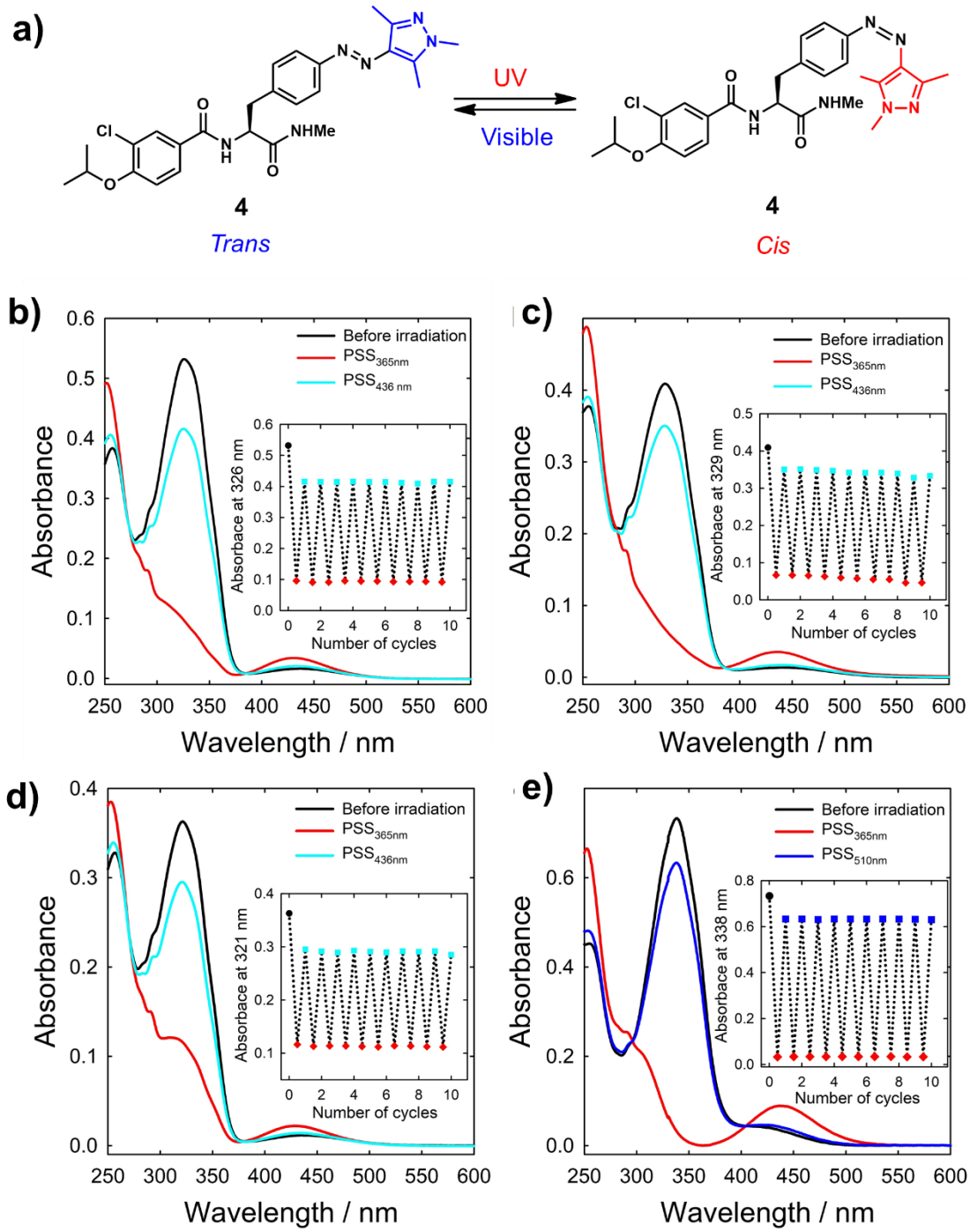

Figure 2-2: a) Photoisomerization of inhibitors under UV (365 nm) and visible (436 nm, 510 nm) light irradiation. UV-Vis absorption spectra of Cenp-E inhibitors: (b), (c), and (d) for compound **1** (2 x 10^{-5} M), **2** (2 x 10^{-5} M), and **3** (2 x 10^{-5} M), respectively in PIPES buffer (pH 6.8): acetonitrile (1:1) solution , (e) for **4** (3.3 x 10^{-5} M) in BRB-80 buffer (pH 6.9):acetonitrile (1:1) solution at room temperature; before irradiation (black line), PSS_{365nm} (red line), PSS_{436nm} (cyan line), PSS_{510nm} (green line). Inset of (b), (c), and (d): Absorbance changes at 326 nm, 329 nm and 321 nm under alternate light irradiations of 365 nm and 436 nm for Cenp-E inhibitors **1**, **2** and **3** respectively an inset of (e) changes at 338 under alternate light irradiations of 365 nm and 510 nm for Cenp-E inhibitors **4** for 10 cycles.

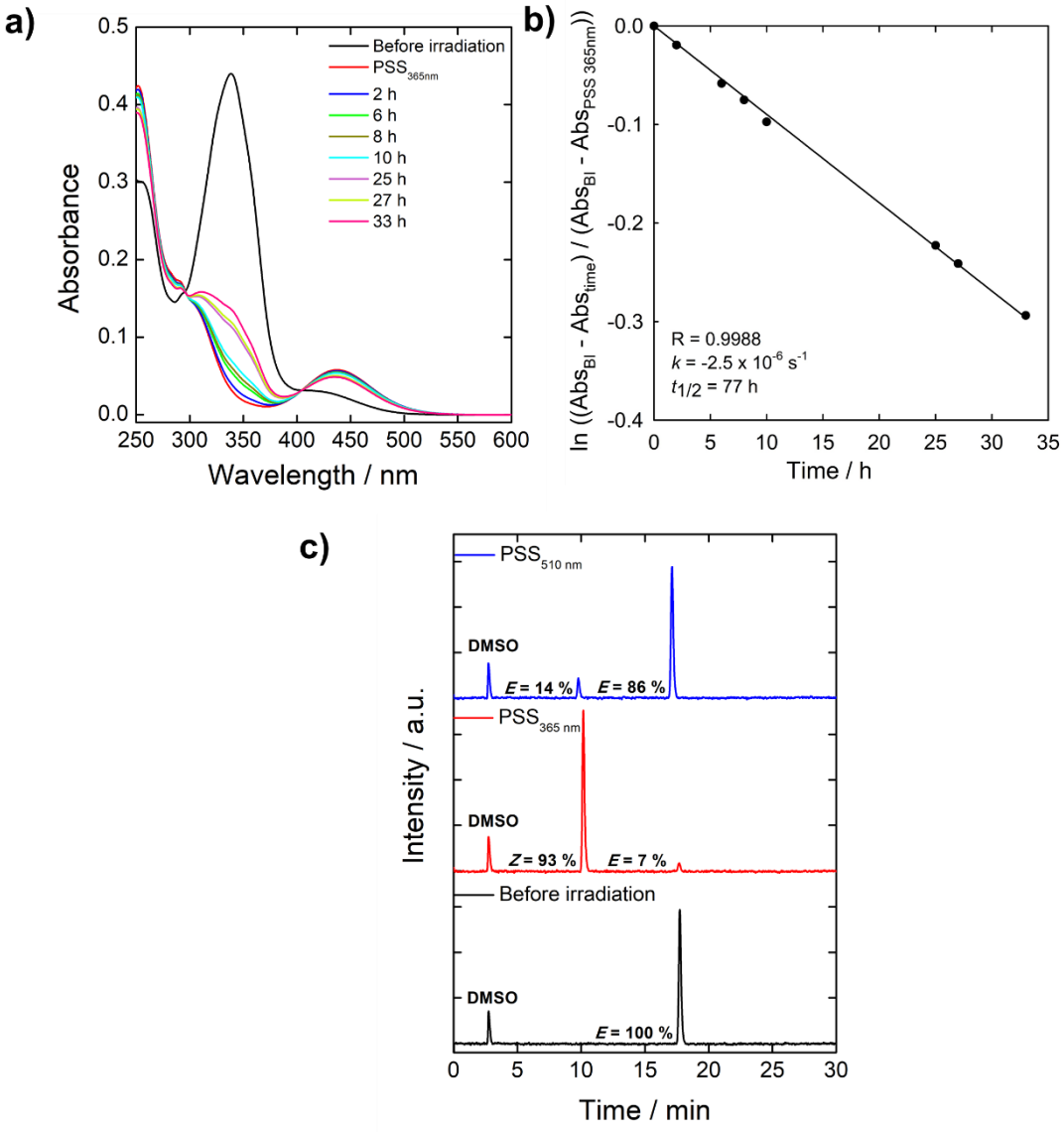

Figure 2-3: (a) Change of the absorption spectra with time after 365 nm light irradiation (PSS_{365nm}) for inhibitor **4** (2.0 x 10^{-5} M) respectively. b) Time course of the absorbance **4** at 339 nm in BRB-80 buffer (pH 6.9):acetonitrile (1:1) solution after UV irradiation and then incubated under dark condition at 37 °C; equation, $\ln(\frac{Abs\ (\mathrm{BI}) - Abs\ (\mathrm{time})}{Abs\ (\mathrm{BI}) - Abs\ (PSS_{365nm})}) = -kt$ was used to determine the rate of the of the thermal isomerization reaction, where *Abs* (BI) is absorbance at before irradiation; *Abs* ($PSS_{365\ nm}$) is absorbance at UV (365 nm) photostationary state; *Abs* (time) is absorbance at different time intervals in dark from PSS_{365nm}. b) RP-HPLC chromatograms for Cenp-E inhibitors **4**, which is showing the *cis* (*Z*) and *trans* (*E*) isomer ratio at before irradiation (black line), PSS_{365nm} (red line), PSS_{510nm} (blue line). Conditions used for the RP-HPLC analysis; Column - 5C18-MS-II, 4.6×250 mm (Nacalai Tesque, Inc.); Eluent - CH_3CN/H_2O, Solvent gradient: 40 to 60% of acetonitrile in water for 30 min; Flow rate: 1 mL/min. Injection volume: 20 µL.

Table 2-1: Ratio of *trans* and *cis* isomers and lifetime of *cis* isomer of photoswitchable inhibitors under different conditions

Cenp-E inhibitors	UV PSS[b]		Visible PSS[c,d]		$t_{1/2}$ / h
	Cis / %	*Trans* / %	*Cis* / %	*Trans* / %	
1	82	18	28	72	55
2	88	12	19	81	32
3	72	28	22	78	85
4	93	7	14	86	77

[a]Ratio was determined at isosbestic point by RP-HPLC (273 nm for **1**, 282 for **2**, 270 nm for **3** and 282 nm for **4**). Life time of all compund measured at 37 °C.
[b]365 nm, [c]436 nm for **1**, **2** and **3**, [d]510 nm for **4**

2.2.3. Reversible Control of Inhibition in Purified Cenp-E

After synthesizing the chemical compounds with desired photophysical properties, I carried out MT stimulated ATPase assay using purified Cenp-E to confirm inhibition behavior. I used the different concentrations of inhibitors, both in the dark state (*trans*) and irradiated state (PSS), together with the positive control GSK923295 and negative control DMSO. As shown in Figure 2-4a, Inhibitor **2** and **3** were inactive toward Cenp-E before and after light irradiation. Inhibitor **1** was less efficient for inhibition at *trans* state compared to *cis* and low solubility in buffer BRB-80 limited it's use. Only inhibitor **4** efficiently inhibited the activity of Cenp-E at low concentration in *trans* state without any solubility problem and activity recovered at *cis* state after UV light irradiation (Figure 2-4b). For inhibitor **4**, I have observed the large difference in inhibitory activity between *trans* and *cis* state and therefore IC_{50} values were determined, showing IC_{50} = 5.9 μM at dark, IC_{50} = 120 μM for PSS_{365nm} and IC_{50} = 14 μM for PSS_{510nm}. Since IC_{50} value 20 times increased at *cis* rich state after UV light irradiation and 9 times decreased at *trans* rich state after visible light irradiation. Whereas GSK923295 did not show any change in inhibitory effect after light irradiation and IC_{50} value is 0.58 μM. These observations confirmed that only inhibitor **4** can reversibly change the inhibition behavior toward Cenp-E using light irradiation. I perused the further all studies using inhibitor **4**.

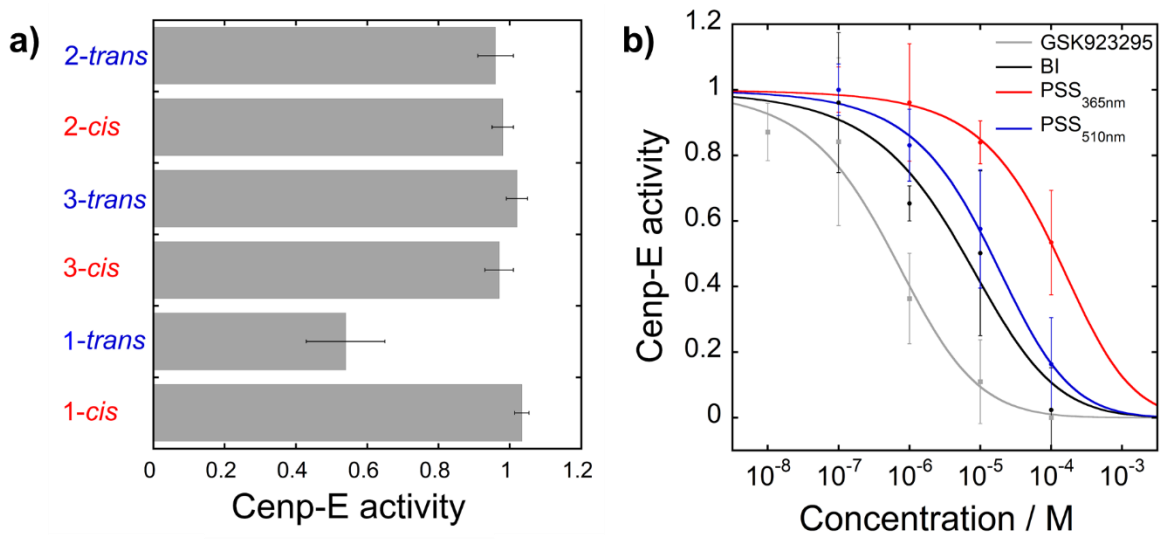

Figure 2-4: a) Change of the activity of Cenp-E in presence of inhibitor **1**, **2** and **3** at *trans* and *cis* rich state b) Concentration dependent inhibition of Cenp-E motor domain ATPase by inhibitor **4** under dark and irradiation (PSS) condition; BI (black line), PSS_{365nm} (red line), PSS_{510nm} (green line) and GSK923295 (gray line).

2.2.4. Inhibition Mechanism of Inhibitor 4

Usually nucleotide free or ATP-bound kinesins tightly bind to the MT, whereas ADP-bound form weakly bind to the MT. In presence of GSK923295, ADP•Pi-bound or ATP-bound form of Cenp-E was stabilized and form rigor state in which inactive Cenp-E motor domain strongly bind to microtubule. Inhibition mechanism of inhibitor **4** can explain by existing mechanism for GSK923295.[17] Here I examined the interaction of Cenp-E motor domain with MT in presence and absence of inhibitor 4 under both dark and irradiation (PSS) state using different nucleotide conditions by copelleting of Cenp-E motor domain with MT (Figure 2-5). Here, in absence of inhibitor **4** and presence of adenylyl-imidodiphosphate (AMPPNP), a poorly hydrolysable ATP analog, or in the nucleotide-free state, Cenp-E motor domain bound tightly to MT and remained to the pellet. When bound to ADP, Cenp-E motor domain bound loosely to

MT and released to the supernatant. In contrast, the addition of inhibitor **4** at *trans* state (dark, PSS_{510nm}) resulted tight binding of Cenp-E motor domain to the MT under all nucleotide states and Cenp-E remained to the pellet. After UV light irradiation, in ADP bound state, loosely bound Cenp-E released to the supernatant and tightly bound to MT in presence of AMPPNP and nucleotide free condition like as inhibitor free state. This analysis indicated that *trans* isomer of inhibitor **4** stabilized the ATP (or ADP.Pi)-bound form by locking Cenp-E in a state strongly bound to MT.

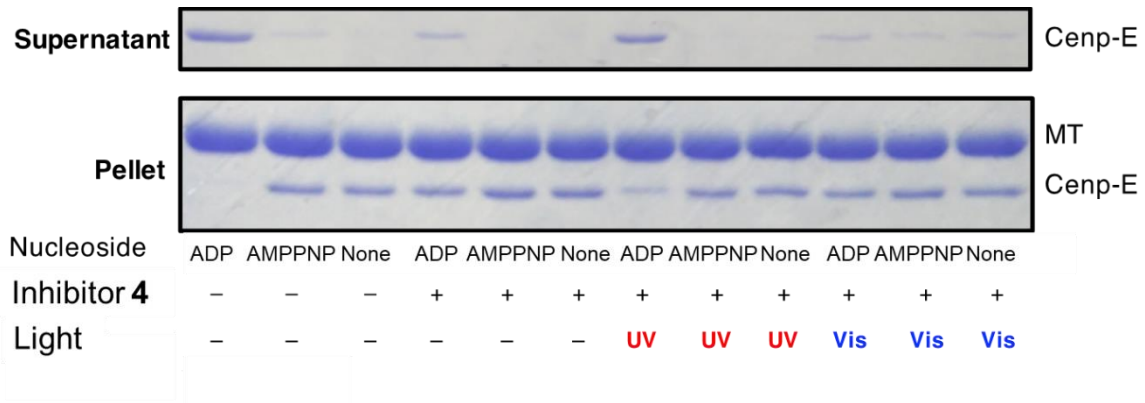

Figure 2-5: Cosedimentation assay of Cenp-E with MT in presence and absence of Cenp-E inhibitor **4** under both dark and irradiation state (PSS) using various nucleotide conditions.

2.2.5. Reversible Control of the Chromosome Movement by Regulating Cenp-E Activity and Ultimate Fate of Living Cells

Generally, transportation of the polar chromosomes along spindle MT towards metaphase plate is driven by positive end directed motor Cenp-E at the kinetochore (Figure 2-6a). Inhibition of Cenp-E stops the movement of chromosomes and induces miscongression of chromosomes in mitotic cells (Figure 2-6b). It is also expected that inhibition of Cenp-E by inhibitor **4** will induce miscongression of chromosomes. To validate the inhibition of inhibitor **4** in living cells, I stained the Cenp-E and α-tubulin by specific antibody and chromosomes by DAPI after treatment with inhibitor **4** along with

positive control GSK923295 and negative control DMSO under dark and irradiation (PSS) conditions. Where α-tubulin and Cenp-E were the marker of mitotic spindles and kinetochore of chromosomes, respectively. At BI and PSS_{510nm} state, majority of cells contained polar localized Cenp-E along with the misaligned chromosomes, proved that *trans* isomer stops the motor activity and Cenp-E mediated chromosome congression (Figure 2-6c). At PSS_{365nm}, Cenp-E were localized to the equator with the perfectly aligned chromosomes, since active Cenp-E transported the chromosomes toward metaphase plate (Figure 2-6c). GSK923295 treated cells contained both aligned and misaligned chromosomes with polar Cenp-E,[17,23] whereas DMSO treated cells contained only the equator positioned Cenp-E along with the completely aligned chromosomes (Figure 2-6d). These results indicate, optochemical tool **4** is promising for specific control of Cenp-E activity in living cells as well as the dynamics of Cenp-E mediated chromosome congression during mitosis cell division.

In response to inhibitor **4** treatment, chromosome miscongression occurred in a concentration dependent manner. As shown in Figure 2-6e, quantitative analysis demonstrated that, at 1 μM concentration, 87% of total cells contain misaligned chromosomes at BI state and reduced to 24% at PSS_{365nm}. At PSS_{510nm}, percent of cells containing misaligned chromosomes recovered to 83%. These observations suggested us, inhibitor **4** can be reversibly and efficiently photoisomerized in cells without photodegradation of drug and induce significant change in chromosome orientation.

Usually miscongression of chromosomes activate SAC protein and induce mitotic arrest. Prolonged mitotic arrest induces cell death. Growth inhibitory effect of inhibitor **4** on HeLa cells were evaluated by a colorimetric assay using cell counting kit-8 (CCK-8, Donjido) based on water soluble tetrazolium salt WST-8 [2-(2-methoxy-

4-nitrophenyl)-3-(4-nitrophenyl)-5-(2,4-disulfophenyl)-2H-tetrazolium, monosodium salt], which is sensitive for the determination of the number of viable cells in cell proliferation assay. WST-8 is reduced by dehydrogenases in cell and produces a water-soluble orange color formazan dye. Amount of the formazan dye is directly proportional to the viable cells, which is detected by measuring the absorbance at 450 nm. Figure 2-6f represented the potency, robustness and light specificity of the Cenp-E inhibitor **4** toward antiproliferative activity of HeLa cells was measured by using a range of concentration of inhibitor **4** (0.01 μM to 20 μM). Negative control confirmed that intensity and time of light irradiation were not toxic for cells. As shown in Figure 2-6f, inhibitor **4** has strong cytotoxicity to HeLa cells in a concentration dependent manner and large difference in cytotoxicity over the PSS_{365nm} and PSS_{510nm} state. *Trans* isomer significantly reduce the viability of cells than the *cis* isomer. A notable difference in growth inhibitory activity (GI_{50}) values, at dark condition GI_{50} is 0.29 ± 0.04 μM, whereas in PSS_{365nm} state it is 2.3 ± 0.3 μM, efficiently reversed by visible light irradiation to 0.29 ± 0.03 μM at PSS_{510nm}. Around 8 times difference in cytotoxicity or GI_{50} values in the *cis* and *trans* rich state. GI_{50} for GSK923295 is 0.03 μM and had no change over cytotoxicity before and after light irradiation (Figure 2-6f). By considering the both change of cell viability and chromosome congression behavior in presence of inhibitor **4**, this is confirming that *trans* isomer potently induce the miscongression of chromosomes, consequently disturb the SAC, and prolonged mitotic arrest induce cell death. By contrast, *cis* isomer induces successful chromosome congression and doesn't involve to induce mitotic arrest. These observations support that, inhibitor **4** can be used as photo trigger which can be

robustly and reversibly photoswitched in living cells between the essentially OFF *cis* from and potent ON *trans* form.

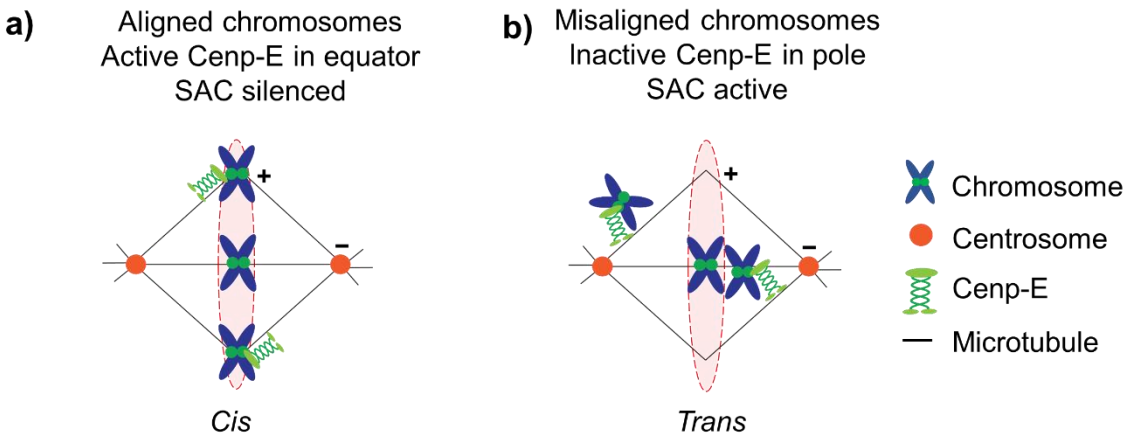

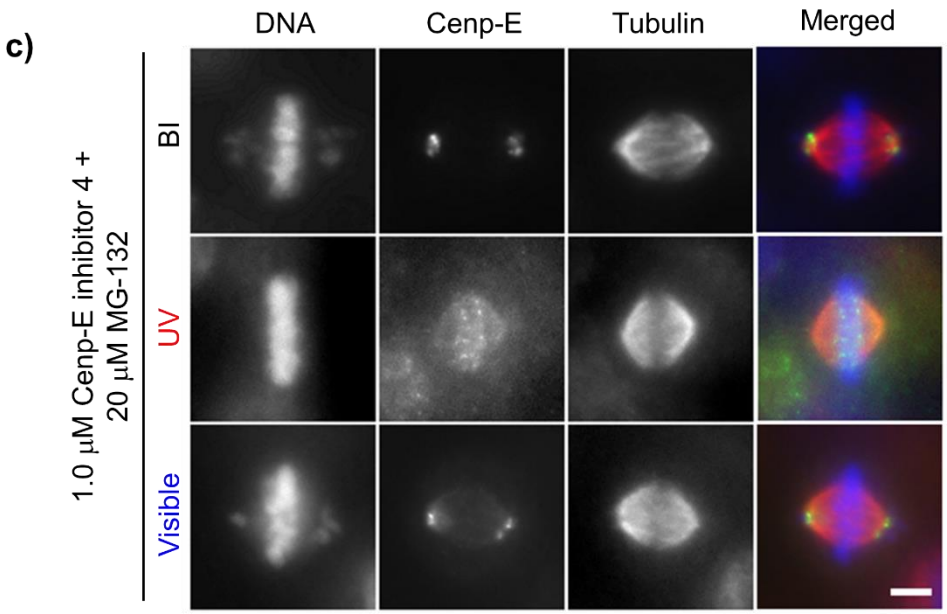

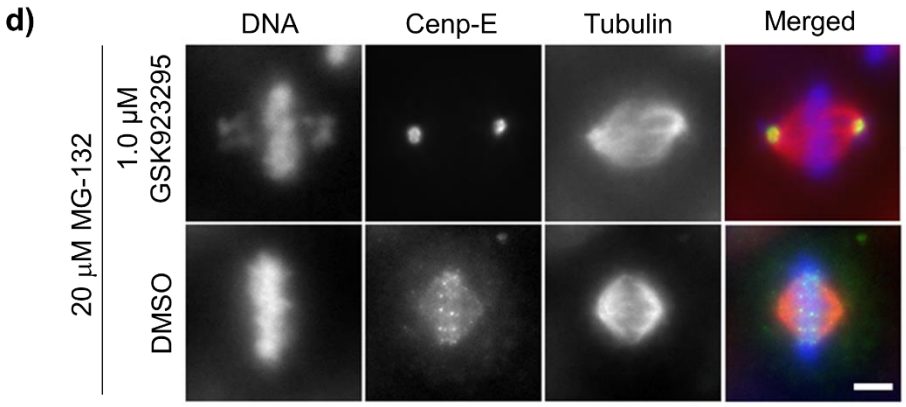

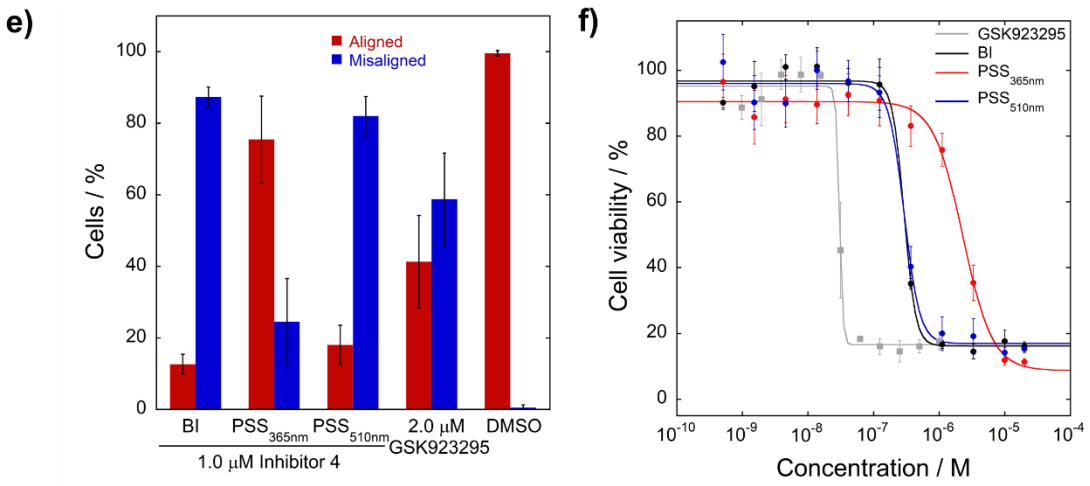

Figure 2-6: (a) Schematic representation of completely-aligned chromosomes in metaphase plate with active Cenp-E. Red dotted ellipse shape indicated metaphase plate. (b) Schematic representation of misaligned chromosomes with inactive Cenp-E. (c) Immunofluorescence analysis of Cenp-E inhibition inside HeLa cells under different irradiation conditions (BI, PSS_{365nm}, PSS_{510nm}). After cells were treated with 1.0 μM inhibitor **4** and 20 μM MG-132 to maintain metaphase stage of cells for 2 h and fixed by methanol at -20 °C, specific antibodies for Cenp-E with Alexa Fluor 488 (green) and tubulin with Alexa Fluor 568 (red) and DAPI for DNA (blue) were applied for staining. Scale bar, 5 μm. d) Representative immunostained images of GSK923295 and DMSO (e) Quantitative analysis of the chromosome amendments of HeLa cells after the treatment of inhibitor **4**, GSK923295 and DMSO at BI, PSS_{365nm} and PSS_{510nm}. Percentage of cells containing aligned and misaligned chromosomes based on n = 3 independent experiments (>150 cells in total). (f) Cell viability assay using GSK923295 (gray line) and inhibitor **4** under at BI (black line), PSS_{365nm} (red line) and PSS_{510nm} (blue line). To maintain the PSS throughout the experimental time, each of UV (2s) and visible (5s) light was irradiated to cells with 12 h interval.

2.2.6. Dynamic Photocontrol of Chromosome Movement in Live Cells

To directly visualize the effect of inhibitor **4** on chromosome movement in living cells under alternating UV and visible light irradiation (Figure 2-7a), I imaged chromosomes. Here, inhibitor **4** treated porcine kidney cell LLC-PK 1 was used for dynamic photoregulation and temporal control of chromosome movement in mitotic cells using light irradiation. After 2h treatment under dark, *trans* isomer generated some misaligned polar chromosomes in mitotic cells (Figure 2-7d). After UV light irradiation (33 mW cm^{-2}, 25 s), active Cenp-E started to transport the misaligned chromosomes toward equator from pole with ~13 nm s^{-1} velocity (Figure 2-7d). Whereas subsequent visible light irradiation (117 mW cm^{-2}, 35 s) stopped the motor activity and induced reverse movement of both kinetochore attached inactive Cenp-E and attached chromosomes with ~3 nm s^{-1} velocity (Figure 2-7d). Here, reverse movement of inactive Cenp-E attached chromosomes occurred due to the MT dynamics. In presence of inhibitor **4** at *trans* state, copelleting assay confirmed (section 2.2.5) inactive Cenp-E tightly bound to the MT (rigor state) and here poleward direction movement of chromosomes occurred due to the treadmilling property of MT (Figure 2-7c). Treadmilling involves the polymerization and depolymerization of equal number of tubulin unit in plus and minus end, respectively. Whereas active Cenp-E at *cis* state processively transfer the chromosome toward the equator by walking on the spindle MT (Figure 2-7b). Figure 2-7e showed the kymograph of moving chromosomes under alternating UV and visible light irradiation. After UV light irradiation, chromosomes moved toward metaphase plate and after visible light irradiation moved far from the metaphase plate. During the repeated cycles of UV and visible light irradiation, gradually number of the misaligned chromosomes decreases. After several cycles, all the chromosomes aligned in the metaphase plate and never

misalign after visible light irradiation (Figure 2-7d, e). Moving distance of chromosomes were vary from cell to cell (Figure 2-7f). Even several misaligned chromosomes in a one cell moved with different velocities. Thus, using this tool, it is possible to control chromosome movement at desired time and position during the cell division.

After complete alignment of chromosomes, function of Cenp-E motor activity at metaphase plate is still controversial. To solve this controversial issue by using this optochemical tool, first I can induce the complete alignment of chromosomes in metaphase plate at *cis* rich state and then inhibit the activity of Cenp-E by subsequent visible light irradiation. After that, I can observe the stability of metaphase plate in presence of polar inactive Cenp-E. These observations assist to find the real function of Cenp-E in metaphase plate after complete alignment of chromosomes.

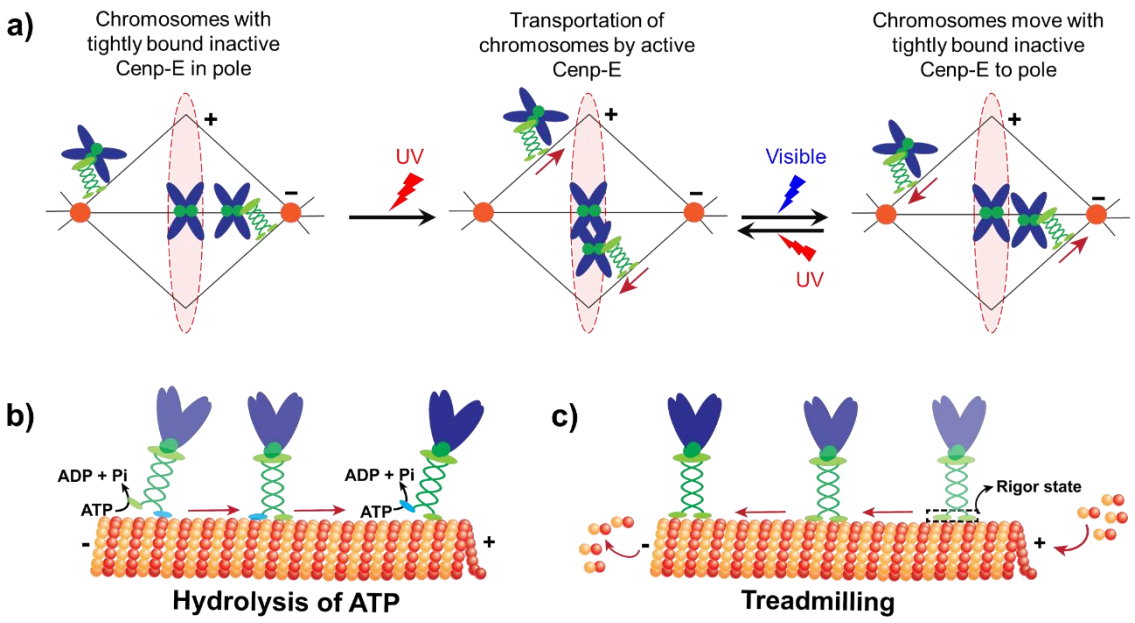

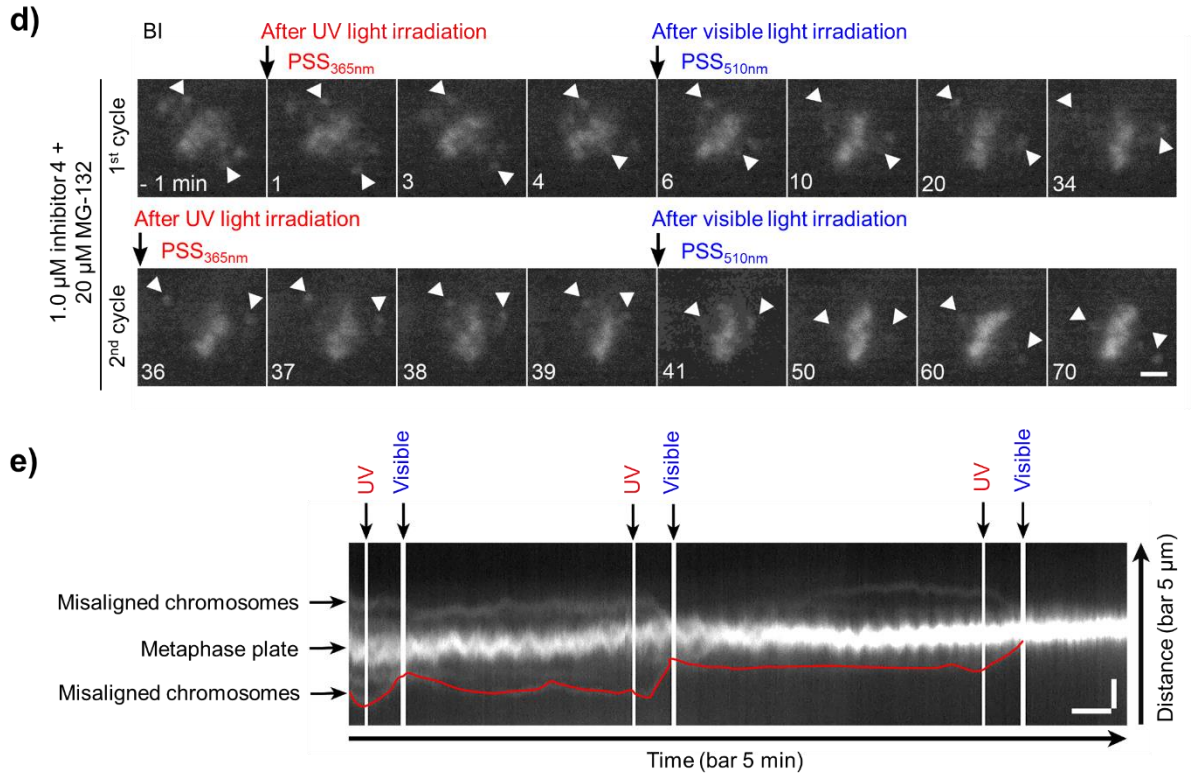
d)
BI
After UV light irradiation
PSS365nm
After visible light irradiation
PSS510nm
1.0 µM inhibitor 4 +
20 µM MG-132
1st cycle
2nd cycle
- 1 min
1
3
4
6
10
20
34
36
37
38
39
41
50
60
70
e)
UV
Visible
Misaligned chromosomes
Metaphase plate
Misaligned chromosomes
Distance (bar 5 µm)
Time (bar 5 min)
f)
Distance / µm
Time / min
Cis
Trans
Cis
Trans
Cis

Figure 2-7: a) Schematic representation of the dynamic photocontrol of chromosome movements using UV and visible light irradiation. b) Schematic representation of active Cenp-E mediated chromosome movement by ATP hydrolysis c) Schematic representation of movement of chromosomes by treadmilling of MT in presence of rigor state of Cenp-E d) Time lapse images of chromosomes in single HeLa cell treated with 1.0 μM inhibitor **4** and 20 μM MG-132 with alternating UV and visible light irradiation. Misaligned chromosomes are marked with white arrows. e) The representative kymograph for the dynamic trace of the misaligned chromosomes around the metaphase plate under different irradiation conditions. Scale bar, 5 μm. f) Change of the distance of moving chromosomes under alternating UV and visible light irradiation based on the 3 independent experiments. Yellow and green box indicated the moving distance after UV and visible light irradiation, respectively. Here I maintained 5 min incubation after UV and 30 min incubation after visible light irradiation.

2.2.7. Temporal Control of the Cenp-E Mediated Chromosome Congression and Function of Cenp-E After Complete Alignment of Chromosomes

Usually bioriented chromosomes takes 15-20 minutes to align at the metaphase plate. To assess the temporal control of the chromosome congression by this optochemical tool, live imaging was done on inhibitor **4** treated HeLa cells by maintaining different incubation time (3, 10, 15, 20, 25 and 30 min) after UV light irradiation (33 mW cm^{-2}, 25 s) and subsequent visible light irradiation (117 mW cm^{-2}, 35 s) and 30 min incubation. During observation, misaligned chromosomes started to move toward the equator from pole after UV light irradiation. After 3 min of UV light irradiation subsequent visible light irradiation induced the reverse movement of chromosomes (Figure 2-8b). This phenomenon mentioned here as a type 1 (Figure 2-

8a). Since elongated incubation time *i.e.* 30 min after UV light irradiation induced complete alignment of chromosomes at metaphase plate, chromosomes never moved to the opposite direction after visible light irradiation (Figure 2-8b) and mentioned as type 2 phenomenon (2-8a). Quantitative analysis showed, with increasing the incubation time after UV light irradiation gradually number of miscongrated chromosomes containing cells or type 1 decreased and type 2 increased (Figure 2-8c). These observations suggested stably attached chromosomes never misalign after inhibition of Cenp-E.

To understand the controversial function of Cenp-E after complete congression of chromosomes at the metaphase plate, I utilized the previously described temporal control of this optochemical tool. Here, I reversely regulated the activity of Cenp-E and checkpoint protein mad2 by using inhibitor **4** (Figure 2-8 d). Generally, in presence of misaligned chromosomes, checkpoint is active and checkpoint proteins localized to kinetochores. After complete alignment of chromosomes at metaphase plate, checkpoint become silenced and proteins are released from all kinetochores at metaphase, leading to anaphase. Already it is proved that, 30 min incubation at *cis* rich state is enough to get complete alignment of chromosomes at metaphase plate. Here immunostained images confirmed that, after 30 min of UV light irradiation, Cenp-E localized to the equator with the completely aligned chromosomes like as DMSO treated cells, since checkpoint became silenced and mad2 detached from the kinetochore (Figure 2-8e,f). These observations ensured further cell cycle progression is possible at *cis* rich state. Notably, subsequent 30 min incubation after visible light irradiation only delocalize the Cenp-E from the equator to pole without any chromosomes and absence of mad2 (Figure 2-8e,f) indicated that after stable

attachment of chromosomes metaphase plate can maintain it's stability without Cenp-E and SAC permitted the cells to proceed anaphase.

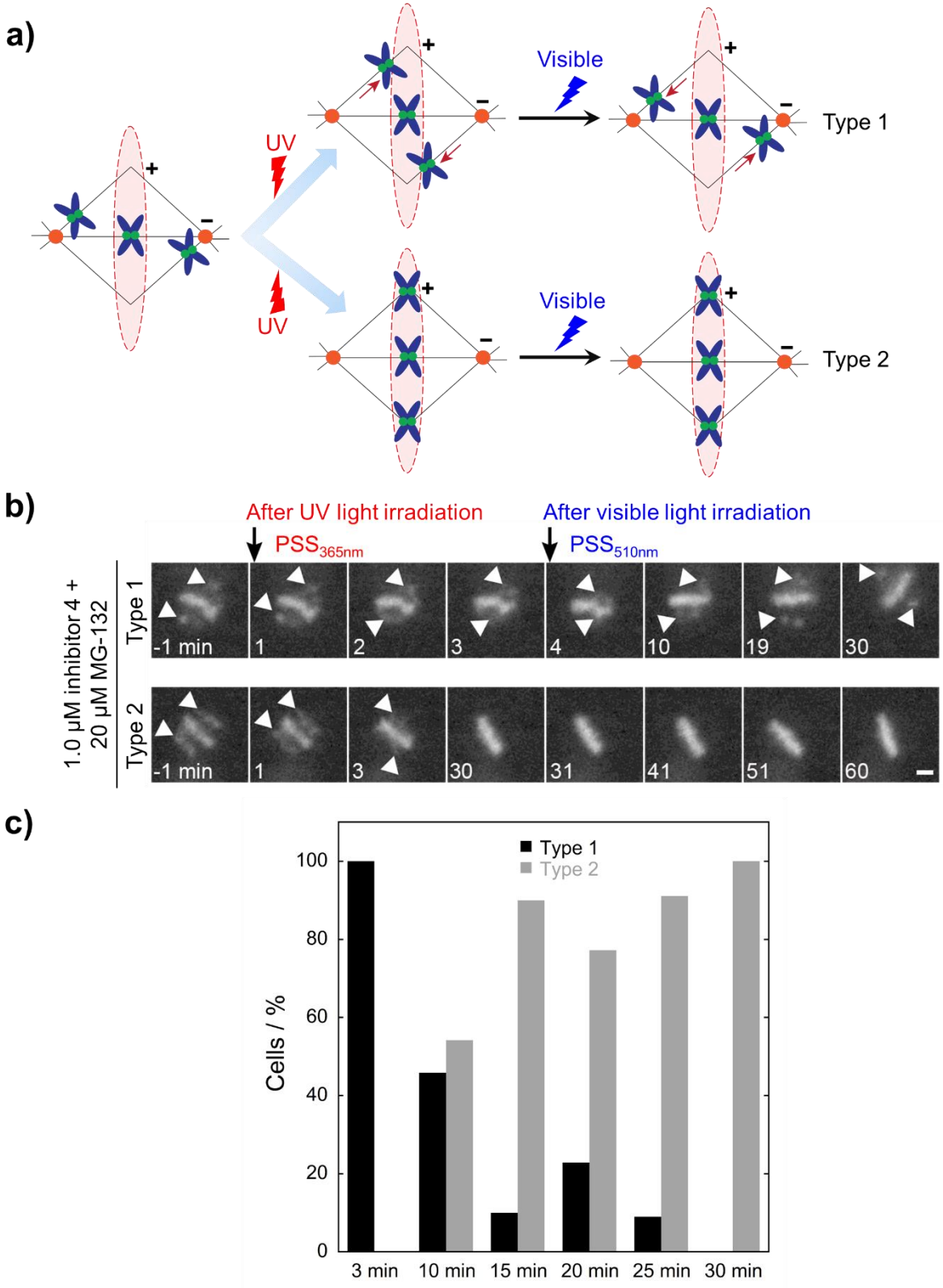

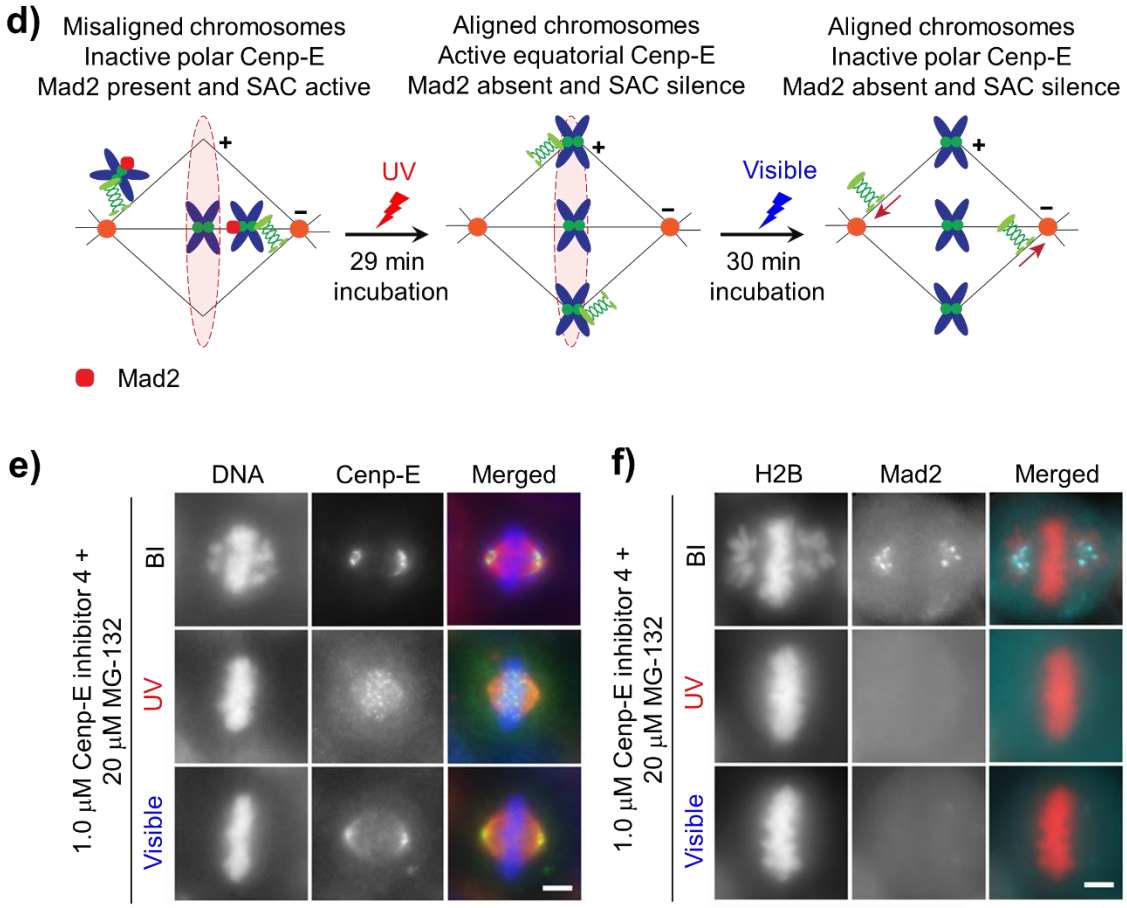

Figure 2-8: (a) Schematic representation of different chromosome movement behavior in presence of active and inactive Cenp-E under UV and subsequent visible light irradiation, respectively. (b) Experimental time lapse images of single cell of type 1/2 depending on the different irradiation conditions. Misaligned chromosomes are marked with white arrows. Scale bar, 5 µm. Type 1: chromosomes moved toward metaphase plate after UV light irradiation and reversely back toward pole after visible light irradiation, Type 2 : chromosomes completely aligned at the metaphase plate after UV light irradiation and never moved to opposite direction after visible light irradiation. (c) Quantitative analysis of cellular population of type 1/2 at different incubation time after UV light irradiation. Percentage of cells containing aligned and misaligned chromosomes based on *n* = 3 independent experiments (>37 cells in total). d) Schematic representation of the control over the movements of Cenp-E and SAC

protein mad2 under UV and visible light irradiation. (d) Representative immunofluorescence images of HeLa cells in type 2. DNA (blue), Cenp-E (green), tubulin (red). e) Fixed cell imaging of stable HeLa-Kyoto cell line of Mad2-GFP and H2B-mCherry in type 2. DNA (red) and cyan (mad2). Scale bar, 5 μm.

2.3. Discussion

I developed a new optochemical tool to control the activity of kinetochore motor protein Cenp-E and helps to explain the exact function of Cenp-E during mitosis cell division. This is the first azobenzene-tethered photoswitchable Cenp-E inhibitor, which can reversibly photoisomerized and significantly changed the binding affinity of two isomers toward the Cenp-E motor domain. By using this system, activity of the Cenp-E can be switched ON and OFF repeatedly for many cycles in living cells, consequently changed the Cenp-E mediated chromosome dynamics in mitotic spindle. These results illustrated that inhibitor **4** potentially suppress and restore the activity of Cenp-E at *trans* and *cis* state, respectively.

Our optochemical tool helps to explore two important parts of mitosis cell division. First by using this tool, it is possible to get temporal control over the activity of Cenp-E and chromosome movement in mitotic spindle by using two different wavelength of light in ON and OFF switching manner. Live imaging proved that active Cenp-E transport the chromosomes from pole to equator under *cis* rich state at UV light irradiation. Whereas inactive and tightly bound Cenp-E transport the chromosomes from equator to pole by using treadmilling property of MT under *trans* rich state after visible light irradiation. Second, I can explain the most controversial issue that the function of Cenp-E after chromosome congression in metaphase plate. Observations from temporal control of chromosome dynamics and localization of Cenp-E and mad2 protein ensured that, in presence of polar inactive Cenp-E at *trans* rich state, completely aligned

chromosomes can maintain their metaphase plate without making any change. It proves that Cenp-E is not necessary for chromosome maintenance after metaphase plate formation.

2.4 Conclusions

I successfully developed an optochemical tool, which can control the chromosome movement reversibly with temporal pre*cis*ion by *cis* and *trans* isomerization. The reversibility of bioactivity by inhibitor **4** allowed quick recovery of normal function of Cenp-E, since cell division also can be controlled by using light at any time and place according to the requirement. I therefore expect that, this optochemical tool will be a promising approach for spatiotemporally precise research based on Cenp-E activity.

2.5. Experimental

2.5.1. General Methods

All reagents, solvents and amino acids were purchased from commercial sources (Sigma Aldrich, TCI chemical, Merck, Kanto Chemical, Wako pure chemical, Watanabe chemical Co. Ltd.) and used without further purification.

Thin layer chromatography was conducted on silica gel 60 F_{254}-precoated aluminium sheets (Merck) and visualized by fluorescence.

For purification of compounds, conventional column chromatography was carried out on silica gel (Kanto chemical, silica gel 60 N, spherical, neutral, 63-210 μm).

Purity and isomer ratio of CENP-E inhibitors were measured by reverse phase high pressure liquid chromatography (RP-HPLC) system (Shimadzu 18886).

Lyophilization (FDU-2200, EYELA) was used for freeze drying.

^{1}H NMR spectra were recorded on a JEOL JNM-ECX 400 spectrometer and all chemical shifts are cited on the δ-scale in ppm relative to the signal of tetramethylsilane (TMS) (at 0.00) as an internal standard and coupling constants (*J*) are reported in Hz.

Proton-decoupled ^{13}C NMR spectra were recorded on a JEOL JNM-ECX 400 spectrometer and all chemical shifts (δ) are reported in ppm using solvent as the internal standard ($CDCl_3$ at 77.16, DMSO-d_6 at 39.52, CD_3OD at 49.00) and relative intensities are also shown.

High resolution mass spactra (HR-MS) was recorded by electrospray ionization (ESI) method using Thermo Scientific Exactive mass spectrophotometer.

UV-vis absorption spectra were measured on a JASCO V-550 spectrophotometer by using 1cm path length quartz cells.

Cis-trans photoisomerization of Cenp-E inhibitors in different experiments was performed by using 365 nm light emitting diode (LED, C11924-101, Hamamatsu), 510 nm (CS-LED3W_510) and for 436 nm, a mercury lamp (ushio) with appropriate bandpass filter.

2.5.2. ATPase Assay for Cenp-E Enzymatic Activity

The ATPase assay activity of Cenp-E was measured based on a reaction in which the regeneration of hydrolyzed ATP is coupled to the oxidation of NADH. In each cycle of ATP hydrolysis, pyruvate kinase (PK) converts one molecule of phosphoenolpyruvate (PEP) to pyruvate system when the ADP is converted back to the ATP. Subsequently pyruvate is converted to lactate by lactate dehydrogenase (LDH) resulting in the oxidation of one NADH molecule. Activity was determined by measuring the the rate

of NADH absorbance decrease at 340 nm, which is proportional to the rate of steady-state ATP hydrolysis. Here, ATPase assay was performed by using 10 nM Cenp-E motor domain, 0.28 mM NADH, 2 mM PEP, PK 19 U/mL, LDH 12 U/mL, MT 2 µM, ATP 500 µM in BRB80 buffer (pH 6.9; PIPES, 80 mM; MgCl2, 2 mM; EGTA, 1 mM) at 25 °C. Absorbance of NADH was measure by UV-visible spectrophotometer (JASCO V-550) at 340nm.

2.5.3. Cell Culture

HeLa-Kyoto (human cervix adenocarcinoma) and LLC-PK1 (Porcine kidney) cell lines were cultured in DMEM (Dulbecco's Modified Eagle Medium, with L-glutamine and phenol red, Wako) cell culture medium supplemented with 10 % FBS (Fetal Bovine Serum, Corning), 1% antibiotic and antimycotic solution (Sigma) at 37 °C in presence of 5% CO_2 and humidified atmosphere. A HeLa-Kyoto line stably expressing Mad2-GFP and H2B-mCherry was a kind gift from Dr. Daniel Gerlich (Institute of Molecular Biotechnology of the Austrian Academy of Sciences and cells were maintained in DMEM supplemented with 10 % FBS (Corning), 1% antibiotic and antimycotic solution (Sigma) 0.5 mg/mL G418 (Wako), and 0.5 µg/mL puromycin.

2.5.4. Cell Viability Assay

Viability of HeLa Kyoto (wild type) cells were evaluated by a colorimetric assay using cell counting kit-8 (CCK-8, Donjido) based on water soluble tetrazolium salt WST-8 [2-(2-methoxy-4-nitrophenyl)-3-(4-nitrophenyl)-5-(2,4-disulfophenyl)-2H-tetrazolium, monosodium salt], which is sensitive for the determination of the number of viable cells in cell proliferation assay. WST-8 is reduced by dehydrogenases in cell and produces a water-soluble orange color formazan dye. Amount of the formazan dye is directly proportional to the viable cells, which is detected by measuring the absorbance at 450

nm. For cell viability assay, 90 µL solution of cells in phenol red free DMEM medium were seeded in three 96 well plates (TrueLine) at 0.15 x 10^5 cells/mL concentration to maintain the three different irradiation conditions: before irradiation (BI, 100 % trans), *cis* rich state (PSS obtained by illumination at 365 nm light) and *trans* rich state (PSS obtained by illumination at 510 nm light). Cells were incubated for 24 h at 37 °C in presence of 5% CO_2 and humidified atmosphere. Solutions of inhibitor 4, GSK923295 (positive control) and DMSO (negative control) in phenol red free DMEM medium with different concentrations were prepared. Before addition to the cell, solutions separately irradiated by UV and visible light to get the PSS_{365nm} and PSS_{510nm} respectively. 10 µL of all solutions were added to the cells and incubated for 44 h. Same concentrations of inhibitor 4 without any cells were also prepared in DMEM medium and measured the absorbance to subtract the contribution of absorbance from azobenzene group of inhibitors. For background wells, only medium also prepared. UV (21 mW cm^{-2}, 2 seconds) and visible (117 mW cm^{-2}, 5 seconds) light was irradiated throughout the dishes with 12 h interval to maintain the *cis* and *trans* rich state of inhibitor 4. After 44 h drug treatment, 5 µL of CCK-8 solution was added to the each well and incubated for 4 h. Absorbance of each well was measured at 450 nm by using Sunrise plate reader (Tecan). Cytotoxicity was expressed as a relative viability of cells compared to the non-treated cells. Presented data are the average of three independent experiment. IC50 values were estimated by a nonlinear regression analysis (four parameter logistic model), where log[inhibitor] were plotted with the percent of activity.

2.5.5. Microscopy and Image Acquisition

Live cell imaging was done by using TE2000 microscope (Nikon) equipped with 20x 0.75 NA Plan-Apochromatic and 60x 1.4 NA Plan-Apochromatic, oil immersion

objective lens (Nikon), an ORCA-ER CCD camera (Hamamatsu Photonics) at 37 °C in presence of 5% CO_2 and humidified atmosphere maintained by microscope stage incubator (TOKAI HIT). Acquisition of image was controlled by µManager software (Open Imaging).

Fixed cells were imaged by Eclipse Ti2 microscope (Nikon) equipped with 20x 0.75 NA Plan-Apochromatic objective lens (Nikon), a Prime 95B camera (Photometrics) at room temperature. Acquisition of image was controlled by NIS Elements software (Nikon).

For immunostaining experiment, z-stacks for chromosome, Cenp-E, and microtubule images were taken with -8 to 8 µm spacing for 4 steps.

To identify the mad2 and H2B in fixed sample, z-stacks for mad2 and H2B images were taken with -10 to10µm spacing for 5 steps.

2.5.6. Antibody

Antibodies were commercially purchased and following antibodies were used for immunostaining with mentioned dilution ratio: primary antibodies are rat monoclonal anti–α-tubulin (1:1000; YOL1/34; EMD Millipore), and mouse monoclonal anti-Cenp-E (1:1000; 1H12, ab5093, Abcam). Alexa Fluor 488 and Alexa Fluor 568 conjugated secondary antibodies (1:1000; Jackson ImmunoResearch Laboratories).

2.5.7. Fixed Cell Imaging

For fixed cell imaging, 500 µL solution of cells in DMEM medium were seeded in three 24 well plates (TrueLine) at 1.0 x 10^5 cells/mL concentration to maintain three different irradiation conditions: BI, *cis* and *trans* rich state and incubated for 24 h. Solutions of inhibitor 4, GSK923295 (positive control) and DMSO (negative control) with 20 µM

MG132 (Peptide Institute) proteasome inhibitor in phenol red free DMEM medium with different concentrations were prepared. Before addition to the cell, solutions separately irradiated by UV and visible light to get the $PSS_{365\ nm}$ and $PSS_{510\ nm}$ respectively. Then cell cultured medium was replaced by the solutions of inhibitor 4 and incubated for 2h. After that, cells were fixed by 3.2% PFA (paraformaldehyde) in DPBS (Dulbecco's phosphate-buffered saline) for 10 min at room temperature and three times washed with DPBS-G (DPBS supplemented with 100 mM glycine). After fixation, chromosomes were stained using 1.0 µg/mL 4',6-diamidino-2-phenylindole (DAPI, Dojindo) for overnight at 4 ºC and washed with DPBS.

To confirm the mad2 position, HeLa-Kyoto (stably expressing Mad2-GFP and H2B-mCherry) cells were seeded in three 4 well glass bottom dish (MATSUNAMI, D141400) at 3.0 x 10^5 cells/mL concentration and incubated for 24 h. Three different dishes were prepared to maintain three different irradiation conditions: BI, *cis* and *trans* rich state. Cells were treated with 1.0 µM concentration of photoswitchable inhibitor 4, GSK923295 and DMSO with 20 µM MG132 proteasome inhibitor and incubated for 2 h subsequently light was directly irradiated on the drug treated cell cultured dish to get the photoswitching effect. After UV light irradiation, cells were incubated for different time intervals (5 and 30 min) and followed by visible light irradiation and incubated for 30 min. Then cells with three different irradiation conditions were fixed by 3.2% PFA in DPBS for 10 min at room temperature and washed with DPBS-G.

2.5.8. Live Cell Imaging

For high resolution live cell imaging, 100 µL of LLC-PK1 cells in phenol red free DMEM medium were seeded in 4 well glass bottom dish (MATSUNAMI, D141400) at 1.5 x 10^5 cells/mL concentration and incubated for 24 h. Then chromosomes were stained

by 1.0 μM SiR-DNA (Cytoskeleton) dye with 25 μM verapamil (efflux pump inhibitor, cytoskeleton) for 2 h at 37 °C and 5% CO_2 in humidified atmosphere. After that cells were washed by phenol red free DMEM and treated with 1.0 μM of photoswitcable inhibitor 4 with 20 μM MG132 proteosome inhibitor for 2 h in dark (without irradiation). Chromosomes were imaged by using Cy5 channel using 60x 1.4 NA Plan-Apochromatic, oil immersion objective lens (Nikon) at 12 frames per minute, where cells were alternatively irradiated by UV (33 mW cm^{-2}, 25 s) and visible (117 mW cm^{-2}, 35 s) light for several cycles.

For low resolution live cell imaging, 100 μL of Hela Kyoto (wild type) cells in phenol red free DMEM medium were seeded in 4 well glass bottom dish at 1.5 x 10^5 cells/mL concentration and incubated for 24 h. Then chromosomes were stained by 0.5 μM SiR-DNA (Cytoskeleton) dye for 2 h. After that cells were washed by phenol red free DMEM and treated with 1.0 μM inhibitor 4 with 20 μM MG132 proteosome inhibitor for 2 h in dark. Chromosomes were imaged by using Cy5 channel at 1 frames per minute, where cells were irradiated by UV (33 mW cm^{-2}, 25 s) and followed by visible (117 mW cm^{-2}, 35 s) light. To get the temporal control of chromosome movement by inhibitor 4, different incubation time intervals (3, 10, 15, 20, 25 and 29 min) after UV light irradiation were maintained.

2.5.9. Immunofluorescence Staining

For immunofluorescence staining 100 μL of Hela Kyoto cells in phenol red free DMEM medium were seeded in 4 well glass bottom dish at 3.0 x 10^5 cells/mL concentration and incubated for 24 h. Three different dishes were prepared to maintain three different irradiation conditions: BI, *cis* rich and *trans* rich state. Cells were treated with 1.0 μM concentrations of photoswitchable drug inhibitor 4, GSK923295 and DMSO

with 20 μM MG132 proteasome inhibitor and incubated for 2 h. To get the photoswitching effect, light was directly irradiated on the drug treated cell cultured dish. After UV light irradiation (33 mW cm^{-2}, 25 s), cells were incubated for different time intervals (5 and 30 min) and followed by visible light irradiation (117 mW cm^{-2}, 35 s) and incubated for 30 min. Then cells with three different irradiation conditions were fixed with 100% methanol at −20 °C for 10 min and three times washed by PBS. Methanol fixed cells were treated with BSA blocking buffer (150 mM NaCl, 10 mM Tris-HCl, pH 7.5, 5% BSA, and 0.1% Tween 20) for 30 min at room temperature followed by incubated with primary antibodies for overnight at 4 °C. After washing, cells were incubated with fluorescence tagged secondary antibodies and DAPI for overnight at 4 °C and three times washed with DPBS. All the antibody solutions were prepared in TBS-BSA buffer.

2.5.10. Synthesis and Characterization

Synthesis of Inhibitor 1

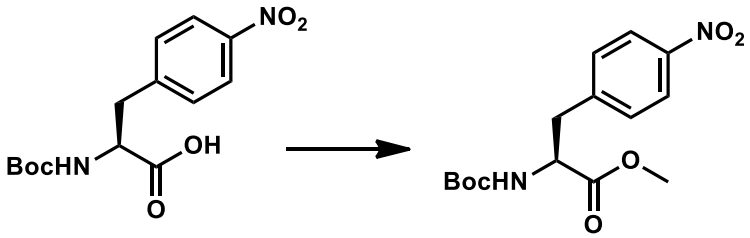

1a

Conditions: MeI, K_2CO_3, DMF, r.t., 22 h

Compound 1a: *N*-(*tert*-Butoxycarbonyl)-4-nitro-L-phenylalanine (503 mg, 1.62 mmol, 1.0 eqv.), methyl iodide (459 mg, 3.24 mmol, 2.0 eqv.) and potassium carbonate (671 mg, 4.85 mmol, 3.0 eqv.) were dissolved in DMF (30 mL). The reaction mixture was stirred at room temperature for 22 h. The mixture poured into EtOAc and washed with water (3 × 100 mL). Organic phase was separated and dried over anhydrous $MgSO_4$.

Evaporation of the solvent afforded the product **1a** as a white solid. Yield: 428 mg, 81%. ^{1}H NMR (400 MHz, $CDCl_3$) δ 8.19 – 8.14 (m, 2H), 7.31 (d, J = 8.7 Hz, 2H), 5.04 (d, J = 6.5 Hz, 1H), 4.66 – 4.61 (m, 1H), 3.74 (s, 3H), 3.28 (dd, J = 14.0, 5.8 Hz, 1H), 3.12 (dd, J = 13.9, 6.4 Hz, 1H), 1.42 (s, 9H). ^{13}C NMR (100 MHz, $CDCl_3$) δ 171.76, 155.03, 147.21, 144.16, 130.36, 123.77, 80.43, 54.20, 52.66, 38.47, 28.35. LR-MS (MALDI-TOF) *m/z*: cacld for $[C_{15}H_{20}N_2O_6 + Na]^+$ 347.1, found 347.2.

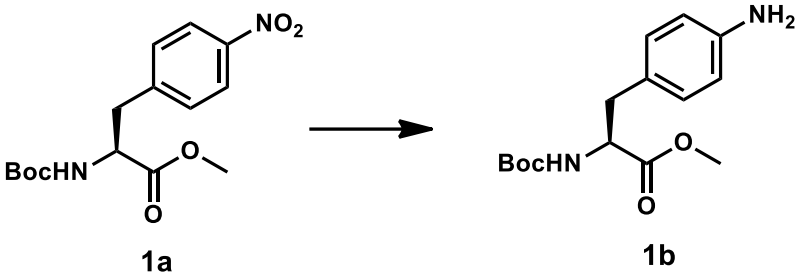

Conditions: Pd/C, H_2 (gas), MeOH, r.t., 25 h

Compound 1b: A solution of **1a** (585 mg, 1.80 mmol) in methanol (10 mL) was stirred with 10% Pd/C (60 mg) catalyst under hydrogen atmosphere at room temperature for 25 h. The reaction mixture filtered through celite and it was concentrated *in vacuo* to afford a sticky colorless oil of **1b**. Yield: 530 mg, 99%. ^{1}H NMR (400 MHz, $CDCl_3$) δ 6.90 (d, J = 8.3 Hz, 2H), 6.63 – 6.60 (m, 2H), 4.94 (d, J = 7.8 Hz, 1H), 4.53 – 4.48 (m, 1H), 3.71 (s, 3H), 3.02 – 2.93 (m, 2H), 1.42 (s, 9H). ^{13}C NMR (100 MHz, $CDCl_3$) δ 172.71, 155.28, 145.44, 130.25, 125.76, 115.41, 79.94, 54.70, 52.26, 37.56, 28.43. LR-MS (MALDI-TOF) *m/z*: cacld for $[C_{15}H_{22}N_2O_4 + Na]^+$ 317.1, found 317.2.

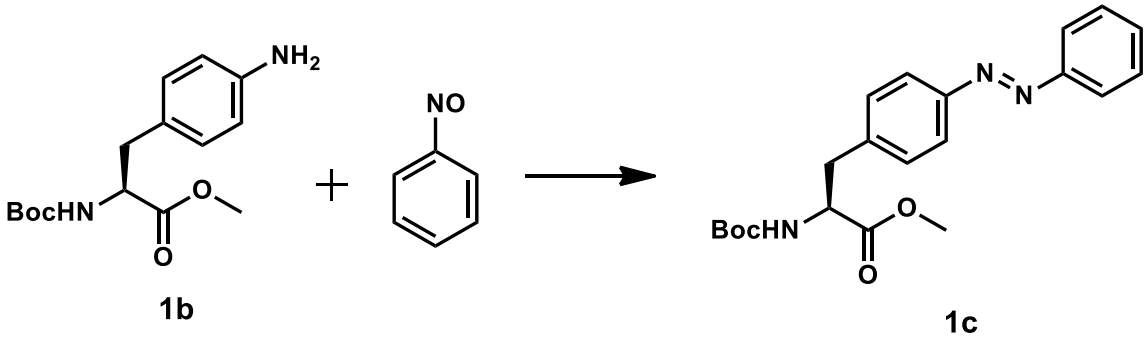

1b **1c**

Conditions: AcOH, r.t., 6 h

Compound 1c: A solution of **1b** (495 mg, 1.68 mmol, 1.0 eqv.) and nitrosobenzene (360 mg, 3.36 mmol, 2.0 eqv.) in acetic acid (5 mL) was stirred at room temperature for 6 h. The reaction mixture was dissolved in DCM. It was extracted with sat. $NaHCO_3$aq and washed with brine. The mixture was dried over $MgSO_4$, filtered and evaporated *in vacuo*. The residual viscous orange oil was purified by column chromatography (Silica, hexane : EtOAc = 2:1) to afford compound **1c** as an orange solid. Yield: 582 mg, 90%. ^{1}H NMR (400 MHz, $CDCl_3$) δ 7.92 – 7.89 (m, 2H), 7.86 (d, J = 8.4 Hz, 2H), 7.54 – 7.45 (m, 3H), 7.28 (d, J = 8.3 Hz, 2H), 5.03 (d, J = 8.0 Hz, 1H), 4.67 – 4.62 (m, 1H), 3.73 (s, 3H), 3.24 – 3.11 (m, 2H), 1.43 (s, 9H). ^{13}C NMR (100 MHz, $CDCl_3$) δ 172.24, 155.17, 152.76, 151.83, 139.50, 131.12, 130.20, 129.22, 123.14, 122.94, 80.21, 54.47, 52.47, 38.39, 28.43. LR-MS (MALDI-TOF) *m/z*: cacld for $[C_{21}H_{25}N_3O_4 + Na]^+$ 406.4, found 406.3.

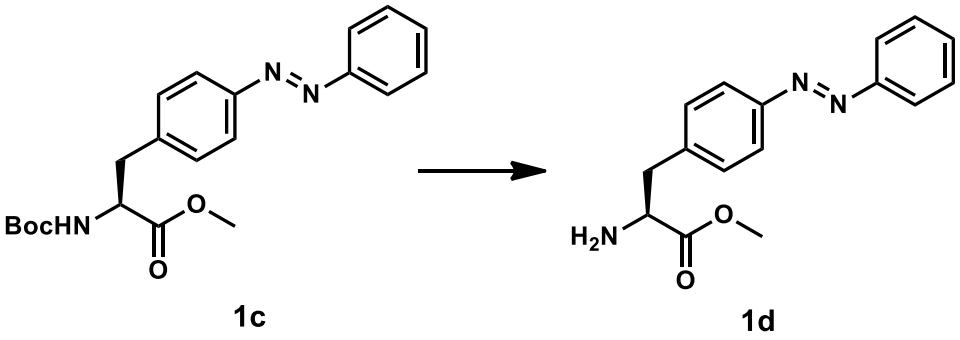

1c **1d**

Conditions: TFA, DCM, r.t., 5 h

Compound 1d: A solution of **1c** (537 mg, 1.40 mmol) in DCM (25 mL) was stirred with TFA (22 mL) at room temperature for 5 h. Evaporation of the reaction mixture afforded the product **1d** as an orange solid. Yield: 397 mg, 100%. ^{1}H NMR (400 MHz, DMSO-d_6) δ 8.44 (br, 2H), 7.91 – 7.86 (m, 4H), 7.62 – 7.58 (m, 3H), 7.48 (d, J = 8.5 Hz, 2H), 4.37 (t, J = 6.7 Hz, 1H), 3.71 (s, 3H), 3.28 – 3.17 (m, 2H). ^{13}C NMR (100 MHz, DMSO-d_6) δ 169.35, 151.93, 151.14, 138.58, 131.61, 130.63, 129.53, 122.78, 122.54, 53.04, 52.70, 35.65. LR-MS (MALDI-TOF) *m/z*: cacld for $[C_{16}H_{17}N_3O_2 + H]^+$ 284.3, found 284.1.

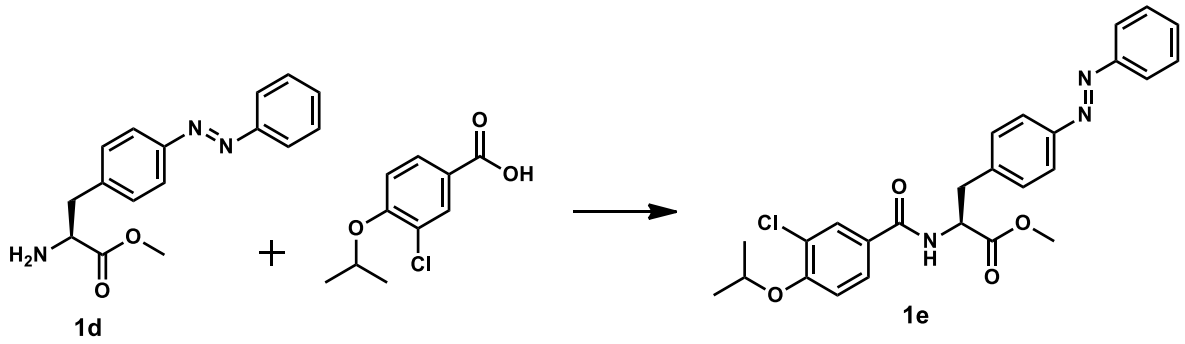

Conditions: HOBT·H_2O, HBTU, DIPEA, DMF, r.t., 15 h

Compound 1e: To a solution of **1d** (450 mg, 1.59 mmol, 1.0 eqv.), 3-chloro-4-isopropoxybenzoic acid[24] (408 mg, 1.90 mmol, 1.2 eqv.), HOBT·H_2O (291 mg, 1.90 mmol, 1.2 eqv.), and HBTU (721 mg, 1.90 mmol, 1.2 eqv.) in DMF (60 mL) was added DIPEA (831 µL, 4.77 mmol, 3.0 eqv.). The reaction mixture was stirred at room temperature for 15 h. EtOAc (40 mL) was added to the reaction mixture. The organic solvent was extracted with sat. $NaHCO_3$aq (100 mL x 3) and washed with brine (100 mL x 3). It was dried over $MgSO_4$, filtered, and evaporated *in vacuo*. The crude mixture

was purified by column chromatography (SiO_2, EtOAc : hexane = 1:2) to afford the product **1e** as an orange solid. Yield: 539 mg, 67%. ^{1}H NMR (400 MHz, $CDCl_3$) δ 7.91 – 7.89 (m, 2H), 7.87 – 7.84 (m, 2H), 7.80 (d, 2.0 Hz, 1H), 7.59 (dd, *J* = 8.0, 2.3 Hz, 1H), 7.54 – 7.47 (m, 3H), 7.29 – 7.27 (m, 1H), 6.94 (d, *J* = 8.8 Hz, 1H), 6.52 (d, *J* = 7.4 Hz, 1H), 5.14 – 5.09 (m, 1H), 4.67 – 4.61 (m, 1H), 3.79 (s, 3H), 3.40 – 3.28 (m, 2H), 1.40 (d, *J* = 6.3 Hz, 6H). ^{13}C NMR (100 MHz, $CDCl_3$) δ 172.02, 165.45, 156.65, 152.71, 151.86, 139.29, 131.16, 130.22, 129.65, 129.22, 126.85, 126.49, 124.14, 123.21, 122.93, 114.19, 72.09, 53.63, 52.72, 37.90, 22.00. LR-MS (MALDI-TOF) *m/z*: cacld for $[C_{26}H_{26}ClN_3O_4 + H]^+$ 480.2, found 480.2.

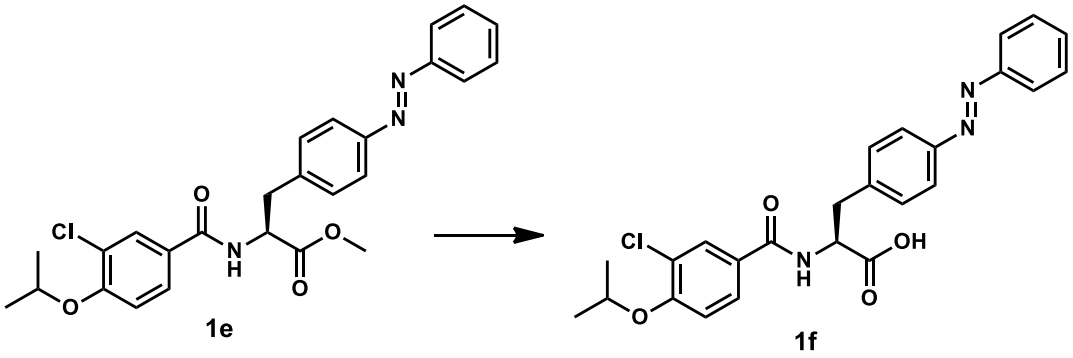

Conditions: NaOH, MeOH, r.t., 9 h

Compound 1f: A solution of **1e** (473 mg, 0.99 mmol) in methanol (35 mL) and 5.0 M NaOH (50 mL) was stirred at room temperature for 9 h. The reaction mixture was evaporated and neutralized by 2.0 M HCl and affording an orange precipitate. The precipitate was filtered and dissolved in EtOAc. The organic solution was extracted with sat. $NaHCO_3$aq (100 mL x 3) and washed with brine (100 mL x 3). It was dried over anhydrous $MgSO_4$, filtered, and evaporated *in vacuo* to afford **1f** as an orange solid. Yield: 462 mg, 98%. ^{1}H NMR (400 MHz, $CDCl_3$) δ 7.91 – 7.86 (m, 4H), 7.77 (d, *J* = 2.3 Hz, 1H), 7.56 (dd, *J* = 8.8, 2.4 Hz, 1H), 7.51 – 7.47 (m, 3H), 7.35 (d, *J* = 8.4

Hz, 2H), 6.92 (d, *J* = 8.9 Hz, 1H), 6.49 (d, *J* = 7.2 Hz, 1H), 5.14 – 5.09 (m, 1H), 4.66 – 4.59 (m, 1H), 3.50 – 3.43 (m, 1H), 3.37 – 3.32 (m, 1H), 1.39 (d, *J* = 6.0 Hz, 6H). ^{13}C NMR (100 MHz, $CDCl_3$) *δ* 174.76, 166.44, 156.88, 152.64, 151.90, 139.15, 131.19, 130.34, 129.71, 129.21, 127.11, 125.87, 124.12, 123.27, 122.97, 114.13, 72.09, 53.78, 37.32, 21.97. LR-MS (MALDI-TOF) *m/z*: cacld for $[C_{25}H_{24}ClN_3O_4 + Na]^+$ 488.1, found 488.2.

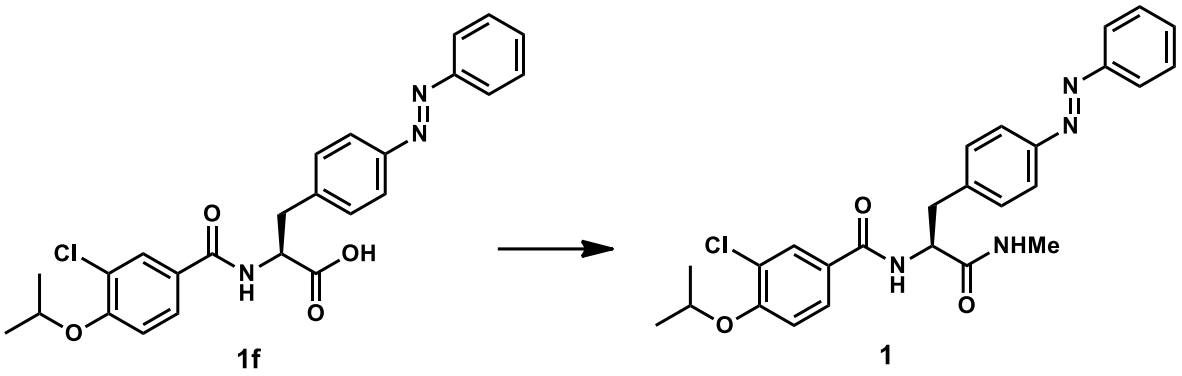

Conditions: $MeNH_2{\cdot}HCl$, HBTU, $HOBT{\cdot}H_2O$, DIPEA, DMF, r.t., 20 h

Compound 1: To a solution of **1f** (413 mg, 0.89 mmol, 1.0 eqv.), methylamine hydrochloride (240 mg, 3.55 mmol, 4.0 eqv.), $HOBT{\cdot}H_2O$ (162 mg, 1.06 mmol, 1.2 eqv.), and HBTU (402 mg, 1.06 mmol, 1.2 eqv.) in DMF (50 mL) was added DIPEA (773 µL, 4.44 mmol, 5.0 eqv.). The reaction mixture was stirred at room temperature for 20 h. EtOAc (40 mL) was added to the reaction mixture. The organic layer was extracted with sat. $NaHCO_3$aq (100 mL x 3) and washed with brine (100 mL x 3). It was dried over $MgSO_4$, filtered and evaporated *in vacuo*. The crude solid was purified by recrystallization (EtOAc: Hexane = 6:1) to afford **1** as an orange solid. Yield: 199 mg, 47%. ^{1}H NMR (400 MHz, $CDCl_3$) *δ* 7.92 – 7.88 (m, 4H), 7.81 (d, *J* = 2.3 Hz, 1H), 7.60 (dd, *J* = 8.6, 2.3 Hz, 1H), 7.55 – 7.46 (m, 3H), 7.43 – 7.41 (m, 2H), 6.94 (d, *J* = 8.8 Hz, 1H), 6.76 (d, *J* = 7.3 Hz, 1H), 5.64 (d, *J* = 4.8 Hz, 1H), 4.81 – 4.75 (m, 1H),

4.67 – 4.61 (m, 1H), 3.34 – 3.29 (m, 1H), 3.18 (dd, *J* = 14.0, 8.4 Hz, 1H), 2.75 (d, *J* = 4.9 Hz, 3H), 1.40 (d, *J* = 6.1 Hz, 6H). ^{13}C NMR (100 MHz, $CDCl_3$) *δ* 171.27, 165.77, 156.72, 152.73, 151.81, 140.13, 131.20, 130.19, 129.75, 129.25, 126.91, 126.31, 124.18, 123.34, 122.98, 114.18, 72.13, 55.18, 38.77, 26.44, 22.02. HR-MS (ESI) *m/z*: calcd for $[C_{26}H_{27}ClN_4O_3 + Na]^+$ 501.16693, found 501.16669.

Synthesis of Inhibitor 2

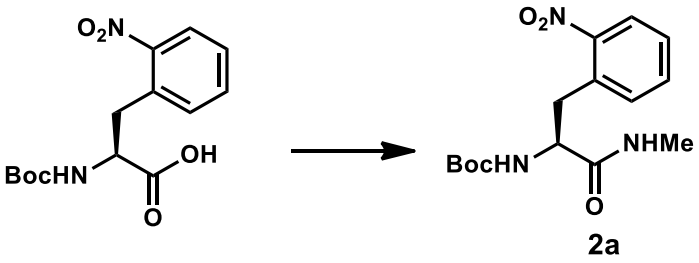

2a

Conditions: $MeNH_2$·HCl, HBTU, HOBT·H_2O, DIPEA, DMF, r.t., 20 h

Compound 2a: To a solution of *N*-(*tert*-butoxycarbonyl)-2-nitro-L-phenylalanine (302 mg, 0.97 mmol, 1.0 eqv.), methylamine hydrochloride (262 mg, 3.87 mmol, 4.0 eqv.), HOBT·H_2O (178 mg, 1.16 mmol, 1.2 eqv.), and HBTU (440 mg, 1.16 mmol, 1.2 eqv.) in DMF (15 mL) was added DIPEA (843 µL, 8.10 mmol, 5.0 eqv.). The reaction mixture was stirred at room temperature for 20 h. EtOAc (30 mL) was added to the reaction mixture. Then organic layer was extracted with sat. $NaHCO_3$aq (100 mL x 3) and washed with brine (100 mL x 3). It was dried over $MgSO_4$, filtered and evaporated *in vacuo* to afford a white solid of **2a**. Yield: 278 mg, 89%. ^{1}H NMR (400 MHz, $CDCl_3$) *δ* 8.00 (d, *J* = 8.4 Hz, 1H), 7.54 (t, *J* = 7.3 Hz, 1H), 7.43 – 7.40 (m, 2H), 6.27 (s, 1H), 5.45 (d, *J* = 8.6 Hz, 1H), 4.58 – 4.54 (m, 1H), 3.50 – 3.46 (m, 1H), 3.08 – 3.03 (m, 1H), 2.83 (d, *J* = 4.6 Hz, 3H), 1.29 (s, 9H). ^{13}C NMR (100 MHz, $CDCl_3$) *δ* 171.71, 155.50,

149.44, 133.32, 132.99, 128.18, 125.29, 80.05, 55.07, 37.18, 28.26, 26.46. LR-MS (MALDI-TOF) *m/z*: cacld for $[C_{15}H_{21}N_3O_5 + Na]^+$ 346.1, found 346.2.

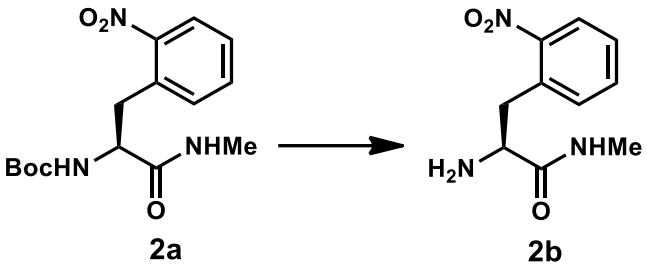

Conditions: TFA, DCM, r.t., 10 h

Compound 2b: A solution of **2a** (270 mg, 0.84 mmol) in DCM (15 mL) was stirred with TFA (8 mL) at room temperature for 10 h. Evaporation of the reaction mixture afforded the product of **2b** as a white solid. Yield: 205 mg, 98%. ^{1}H NMR (400 MHz, DMSO-d_6) δ 8.50 (s, 2H), 8.20 (q, J = 4.3 Hz, 1H), 8.10 (dd, J = 8.2, 1.2 Hz, 1H), 7.73 – 7.69 (m, 1H), 7.60 – 7.56 (m, 1H), 7.39 – 7.37 (m, 1H), 4.02 (s, 1H), 3.47 (dd, J = 14.0, 5.6 Hz, 1H), 3.18 (dd, J = 13.2, 9.3 Hz, 1H), 2.47 (d, J = 4.6 Hz, 3H). ^{13}C NMR (100 MHz, DMSO-d_6) δ 167.82, 148.82, 133.82, 133.22, 130.03, 129.09, 125.17, 52.70, 34.40, 25.43. LR-MS (MALDI-TOF) *m/z*: cacld for $[C_{10}H_{13}N_3O_3 + H]^+$ 224.1, found 224.1.

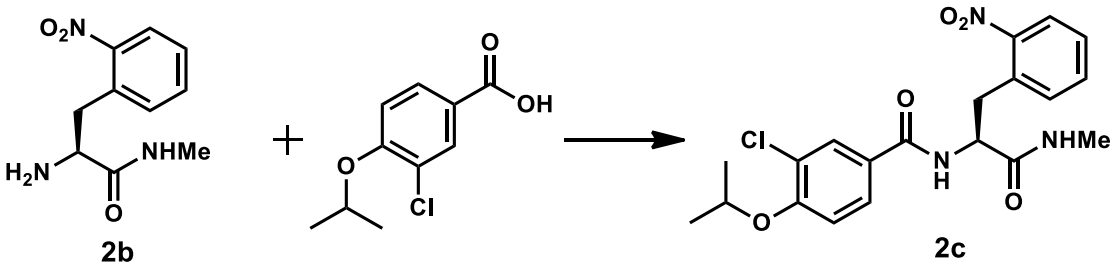

Conditions: HOBT·H_2O, HBTU, DIPEA, DMF, r.t. 25 h

Compound 2c: To a solution of **2b** (199 mg, 0.89 mmol, 1.0 eqv.), 3-chloro-4-isopropoxybenzoic acid[24] (230 mg, 1.06 mmol, 1.2 eqv.), HOBT·H_2O(163 mg, 1.06 mmol, 1.2 eqv.), and HBTU (402 mg, 1.06 mmol, 1.2 eqv.) in DMF (30 mL) was added DIPEA (465 µL, 2.67 mmol, 3.0 eqv.). The reaction mixture was stirred at room temperature for 25 h. EtOAc (20 mL) was added to the reaction mixture. Then organic layer was extracted with sat. $NaHCO_3$aq (100 mL x 3) and washed with brine (100 mL x 3). It was dried over $MgSO_4$, filtered and evaporated *in vacuo.* The crude mixture was purified by column chromatography (SiO_2, EtOAc : hexane = 3:1) to afford the product **2c** as a white solid. Yield: 266 mg, 71%. ^{1}H NMR (400 MHz, $CDCl_3$) δ 7.97 – 7.95 (m, 1H), 7.75 (d, *J* = 2.3 Hz, 1H), 7.55 – 7.51 (m, 2H), 7.42 (d, *J* = 7.6 Hz, 2H), 7.20 (d, *J* = 7.5 Hz, 1H), 6.90 (d, *J* = 8.7 Hz, 1H), 6.31 (d, *J* = 4.7 Hz, 1H), 4.99 – 4.93 (m, 1H), 4.65 – 4.59 (m, 1H), 3.52 (dd, *J* = 13.8, 4.4 Hz, 1H), 3.30 (dd, *J* = 13.9, 10.1 Hz, 1H), 2.85 (d, *J* = 4.9 Hz, 3H), 1.39 (d, *J* = 6.1 Hz, 6H). ^{13}C NMR (100 MHz, $CDCl_3$) δ 171.48, 166.04, 156.66, 149.73, 133.60, 132.96, 132.69, 129.81, 128.46, 126.70, 125.99, 125.30, 124.08, 114.03, 72.09, 54.67, 35.66, 26.58, 22.01. LR-MS (MALDI-TOF) *m/z*: cacld for $[C_{20}H_{22}ClN_3O_5 + Na]^+$ 442.1, found 442.2.

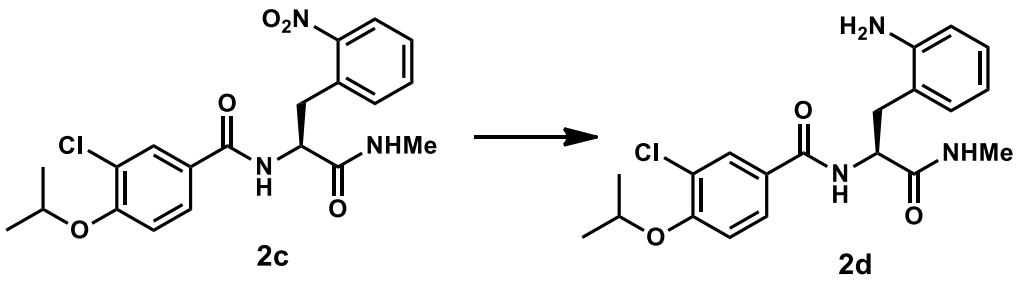

Conditions: Pd/C, H_2 (gas), MeOH, r.t., 2 h

Compound 2d: A solution of **2c** (138 mg, 0.33 mmol) in methanol (5 mL) was stirred with 10% Pd/C (18 mg) catalyst under hydrogen atmosphere at room temperature for

2 h. The reaction mixture filtered through celite and concentrated *in vacuo* afforded a solid compound of **2d**. Yield: 130 mg, 98%. ^{1}H NMR (400 MHz, $CDCl_3$) δ 7.81 – 7.78 (m, 2H), 7.65 (d, J = 8.3 Hz, 1H), 7.15 – 7.06 (m, 3H), 6.94 – 6.85 (m, 2H), 6.78 (s, 1H), 6.27 (br, 2H), 4.97 – 4.92 (m, 1H), 4.64 – 4.55 (m, 1H), 3.23 (d, J = 5.3 Hz, 2H), 2.72 (d, J = 4.5 Hz, 3H), 1.38 (d, J = 6.0 Hz, 6H). ^{13}C NMR (100 MHz, $CDCl_3$) δ 171.97, 166.46, 156.58, 138.76, 131.68, 129.89, 128.57, 127.12, 125.83, 125.52, 123.84, 123.09, 119.80, 113.88, 71.98, 53.48, 34.99, 26.34, 21.95. LR-MS (MALDI-TOF) *m/z*: cacld for $[C_{20}H_{24}ClN_3O_3 + Na]^+$ 412.1, found 412.1.

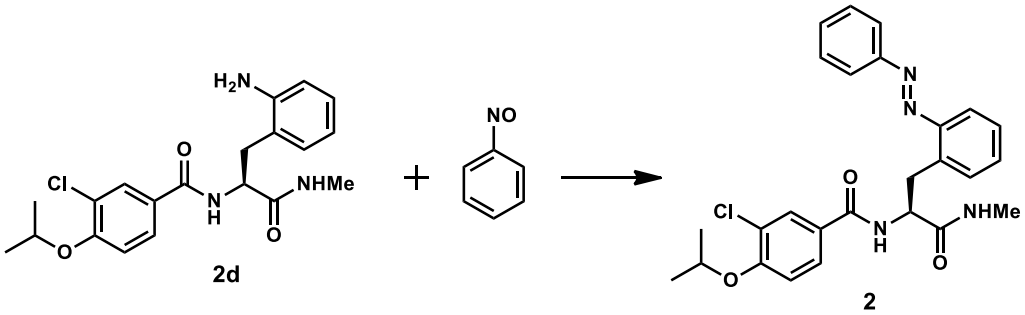

Conditions: AcOH, r.t., 14 h

Compound 2: A solution of **2d** (226 mg, 0.56 mmol, 1.0 eqv.) and nitrosobenzene (119 mg, 1.11 mmol, 2.0 eqv.) in acetic acid (1.3 mL) was stirred at room temperature for 14 h. The reaction mixture was dissolved in EtOAc. It was extracted with sat. $NaHCO_3$aq (100 mL x 3) and washed with brine (100 mL x 3). The mixture was dried over $MgSO_4$, filtered and evaporated *in vacuo*. The residual orange solid was roughly purified by column chromatography (Silica, hexane : EtOAc = 1:9). Final purification was done by using reverse-phase HPLC with a mobile phase gradient (acetonitrile / water with 0.1% TFA = 65 to 100% of acetonitrile in water for 55 min) to afford compound **2** as an orange solid. Yield: 42 mg, 15%. ^{1}H NMR (400 MHz, $CDCl_3$) δ 7.96 – 7.93 (m, 2H), 7.79 – 7.77 (m, 1H), 7.58 – 7.51 (m, 4H), 7.47 – 7.43 (m, 2H), 7.38 –

7.28 (m, 3H), 6.55 (d, *J* = 8.8 Hz, 1H), 6.24 (d, *J* = 4.1 Hz, 1H), 4.82 – 4.76 (m, 1H), 4.53 – 4.47 (m, 1H), 3.88 (dd, *J* = 14.0, 9.1 Hz, 1H), 3.54 (dd, *J* = 13.6, 5.3 Hz, 1H), 2.73 (d, *J* = 4.9 Hz, 3H), 1.34 (dd, *J* = 6.0, 2.3 Hz, 6H).^{13}C NMR (100 MHz, $CDCl_3$) *δ* 171.63, 166.32, 156.42, 152.83, 150.58, 137.44, 131.99, 131.84, 131.72, 129.60, 129.53, 128.17, 126.67, 126.06, 123.98, 123.28, 116.06, 113.77, 71.96, 56.13, 32.74, 26.38, 21.97. HR-MS (ESI) *m/z*: calcd for $[C_{26}H_{27}ClN_4O_3 + Na]^+$ 501.16693, found 501.16635.

Synthesis of Inhibitor 3

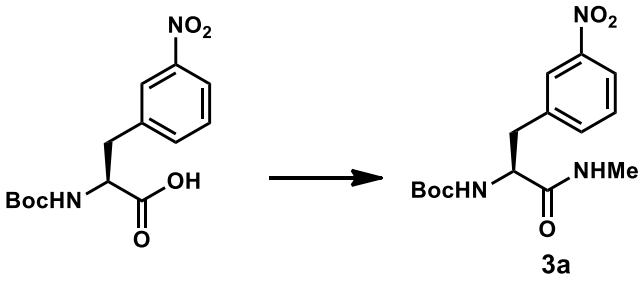

3a

Conditions: $MeNH_2 \cdot HCl$, HBTU, $HOBT \cdot H_2O$, DIPEA, DMF, r.t., 24 h

Compound 3a: To a solution of *N*-(*tert*-butoxycarbonyl)-3-nitro-L-phenylalanine (300 mg, 0.97 mmol, 1.0 eqv.), methylamine hydrochloride (261 mg, 3.87 mmol, 4.0 eqv.), $HOBT \cdot H_2O$(178 mg, 1.16 mmol, 1.2 eqv.), and HBTU (440 mg, 1.16 mmol, 1.2 eqv.) in DMF (15 mL) was added DIPEA (843 µL, 8.10 mmol, 5.0 eqv.). The reaction mixture was stirred at room temperature for 24 h. EtOAc (30 mL) was added to the reaction mixture. Then organic layer was extracted with sat. $NaHCO_3$aq (100 mL x 3) and washed with brine (100 mL x 3). It was dried over $MgSO_4$, filtered and evaporated *in vacuo* to afford a white solid of **3a**. Yield: 153 mg, 49%. ^{1}H NMR (400 MHz, $CDCl_3$) *δ* 8.09 (d, *J* = 7.8 Hz, 2H), 7.57 – 7.54 (m, 1H), 7.48 – 7.44 (m, 1H), 6.42 (s, 1H), 5.31 (d, *J* = 8.7 Hz, 1H), 4.46 – 4.41 (m, 1H), 3.27 – 3.22 (m, 1H), 3.08 – 3.03 (m, 1H), 2.77 (d, *J* = 4.7 Hz, 3H), 1.36 (s, 9H). ^{13}C NMR (100 MHz, $CDCl_3$) *δ* 171.43, 155.64, 148.36,

139.27, 135.81, 129.50, 124.33, 122.10, 80.59, 55.54, 38.52, 28.31, 26.34. LR-MS (MALDI-TOF) *m/z*: cacld for $[C_{15}H_{21}N_3O_5 + Na]^+$ 346.1, found 346.2.

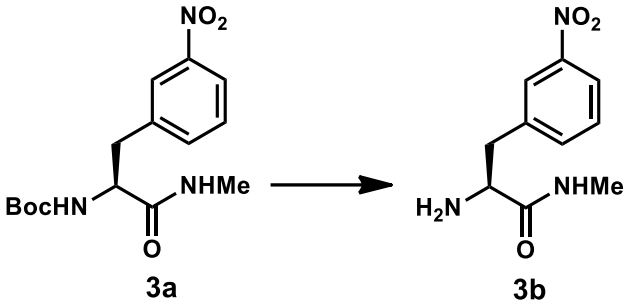

Conditions: TFA, DCM, r.t., 6 h

Compound 3b: A solution of **3a** (118 mg, 0.36 mmol) in DCM (15 mL) was stirred with TFA (10 mL) at room temperature for 6 h. Evaporation of the reaction mixture afforded the product **3b** as a white solid. Yield: 110 mg, 98%. ^{1}H NMR (400 MHz, DMSO-d_6) δ 8.11 – 8.06 (m, 2H), 7.85 (d, J = 3.8 Hz, 1H), 7.67 (d, J = 7.6 Hz, 1H), 7.57 (t, J = 8.0 Hz, 1H), 3.02 (dd, J = 13.3, 5.0 Hz, 1H), 2.78 (dd, J = 13.3, 8.3 Hz, 1H), 2.57 (d, J = 4.6 Hz, 3H). ^{13}C NMR (100 MHz, DMSO-d_6) δ 174.49, 147.59, 141.43, 136.39, 129.41, 123.98, 121.16, 56.08, 25.44. LR-MS (MALDI-TOF) *m/z*: cacld for $[C_{10}H_{13}N_3O_3 + Na]^+$ 246.1, found 246.1.

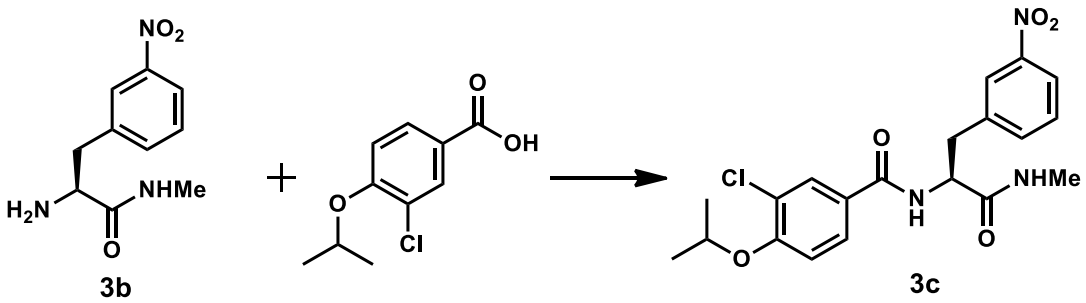

Conditions: HOBT·H_2O, HBTU, DIPEA, DMF, r.t., 25 h

Compound 3c: To a solution of **3b** (103 mg, 0.46 mmol, 1.0 eqv.), 3-chloro-4-isopropoxybenzoic acid[24] (119 mg, 0.55 mmol, 1.2 eqv.), HOBT·H_2O (84 mg, 0.55 mmol, 1.2 eqv.), and HBTU (209 mg, 0.55 mmol, 1.2 eqv.) in DMF (20 mL) was added DIPEA (240 µL, 1.38 mmol, 3.0 eqv.). The reaction mixture was stirred at room temperature for 25 h. EtOAc (20 mL) was added to the reaction mixture. The organic layer was extracted with sat. $NaHCO_3$aq (100 mL x 3) and washed with brine (100 mL x 3). It was dried over $MgSO_4$, filtered and evaporated *in vacuo.* The crude mixture was purified by column chromatography (SiO_2, EtOAc : hexane = 3:1) to afford the product **3c** as a white solid. Yield: 266 mg, 69%. ^{1}H NMR (400 MHz, $CDCl_3$) δ 8.15 – 8.14 (m, 1H), 8.12 – 8.09 (m, 1H), 7.77 (d, *J* = 2.3 Hz, 1H), 7.60 – 7.57 (m, 2H), 7.48 (t, *J* = 7.9 Hz, 1H), 6.92 – 6.86 (m, 2H), 6.14 (q, *J* = 4.8 Hz, 1H), 4.89 – 4.83 (m, 1H), 4.68 – 4.59 (m, 1H), 3.36 – 3.23 (m, 2H), 2.78 (d, *J* = 4.9 Hz, 3H), 1.40 (dd, *J* = 6.0, 2.0 Hz, 6H). ^{13}C NMR (100 MHz, $CDCl_3$) δ 171.08, 166.04, 156.83, 148.43, 138.94, 135.73, 129.75, 129.68, 126.89, 125.95, 124.42, 124.17, 122.34, 114.08, 72.14, 54.71, 38.26, 26.47, 22.02. LR-MS (MALDI-TOF) *m/z*: cacld for $[C_{20}H_{22}ClN_3O_5 + Na]^+$ 442.1, found 442.2.

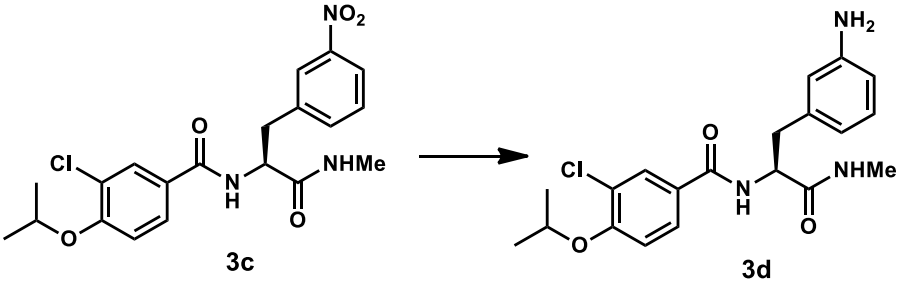

Conditions: Pd/C, H_2 (gas), MeOH, r.t., 2 h

Compound 3d: A solution of **3c** (242 mg, 0.58 mmol) in methanol (10 mL) was stirred with 10% Pd/C (40 mg) catalyst under hydrogen atmosphere at room temperature for 6 h. The reaction mixture filtered through celite and concentrated in *vacuo* to afford a

white solid **3d**. Yield: 221 mg, 98%. R_f = 0.1 (Silica, Hexane: EtOAc = 1:6). This crude product is used for next step without further purification.

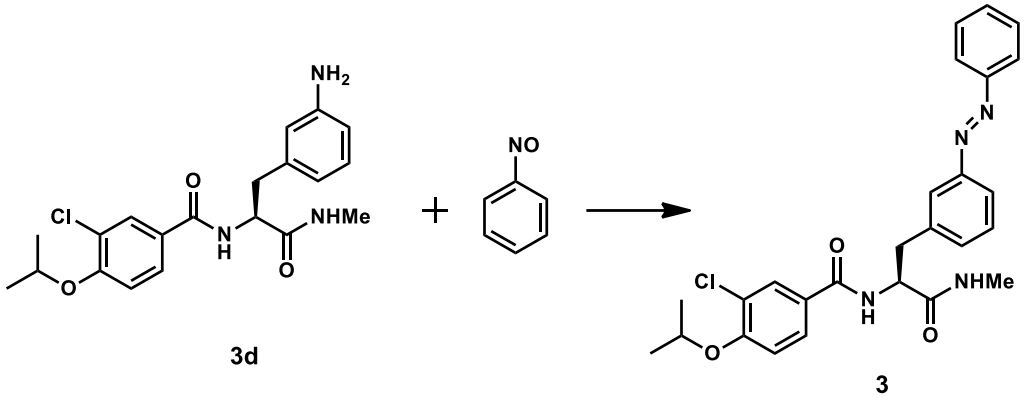

3d 3

Conditions: AcOH, r.t., 14 h

Compound 3: A solution of **3d** (239 mg, 0.59 mmol, 1.0 eqv.) and nitrosobenzene (126 mg, 1.17 mmol, 2.0 eqv.) in acetic acid (1.5 mL) was stirred at room temperature for 14 h. The reaction mixture was dissolved in EtOAc. It was extracted with sat. $NaHCO_3$aq (100 mL x 3) and washed with brine (100 mL x 3). The mixture was dried over $MgSO_4$, filtered and evaporated *in vacuo*. The residual orange solid was roughly purified by column chromatography (Silica, hexane : EtOAc = 1:9). The subsequent purification using reverse-phase HPLC with a mobile phase gradient (acetonitrile / water with 0.1% TFA = 65 to 100% of acetonitrile in water for 55 min) to afford compound **3** as an orange solid. Yield: 193 mg, 68%. ^{1}H NMR (400 MHz, $CDCl_3$) δ 7.91 – 7.88 (m, 2H), 7.83 – 7.79 (m, 3H), 7.59 (dd, J = 8.8, 2.4 Hz, 1H), 7.54 – 7.45 (m, 4H), 7.39 – 7.37 (m, 1H), 6.89 –6.83 (m, 2H), 5.91 – 5.88 (m, 1H), 4.86 – 4.80 (m, 1H), 4.64 – 4.55 (m, 1H), 3.34 (dd, J = 13.6, 6.2 Hz, 1H), 3.23 (dd, J = 13.6, 8.0 Hz, 1H), 2.75 (d, J = 4.9 Hz, 3H), 1.38 (d, J = 6.1 Hz, 6H).^{13}C NMR (100 MHz, $CDCl_3$) δ 171.56, 165.95, 156.60, 152.93, 152.63, 138.08, 132.03, 131.23, 129.80, 129.53, 129.21, 126.94, 126.39, 124.05, 123.25, 123.01, 122.36, 114.05, 72.05, 55.17, 38.65,

26.38, 22.00. HR-MS (ESI) *m/z*: calcd for $[C_{26}H_{27}ClN_4O_3 + Na]^+$ 501.16693, found 501.16641.

Synthesis of Inhibitor 4

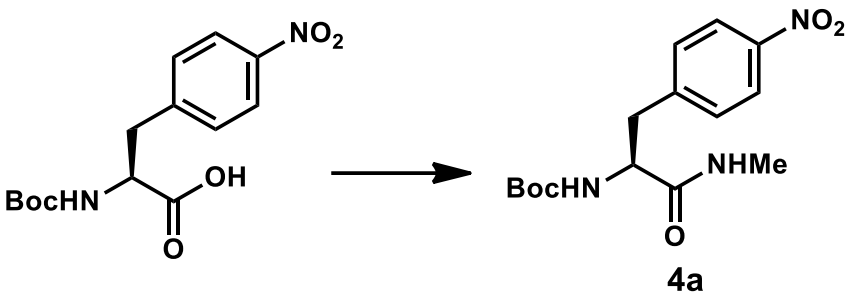

4a

Conditions: $MeNH_2 \cdot HCl$, HBTU, $HOBT \cdot H_2O$, DIPEA, DMF, r.t., 20 h

Compound 4a: To a solution of *N*-(*tert*-butoxycarbonyl)-4-nitro-L-phenylalanine (502 mg, 1.62 mmol, 1.0 eqv.), methylamine hydrochloride (238 mg, 6.48 mmol, 4.0 eqv.), $HOBT \cdot H_2O$ (297 mg, 1.16 mmol, 1.2 eqv.), and HBTU (736 mg, 1.94 mmol, 1.2 eqv.) in DMF (20 mL) was added DIPEA (1.41 mL, 8.10 mmol, 5.0 eqv.). The reaction mixture was stirred at room temperature for 20 h. It was extracted with EtOAc (50 mL) and sat. $NaHCO_3$aq (100 mL x 3) and washed with brine (100 mL x 3). It was dried over $MgSO_4$, filtered and evaporated *in vacuo* to afford a white solid of **4a**. Yield: 483 mg, 92%. ^{1}H NMR (400 MHz, $CDCl_3$) δ 8.15 (d, J = 8.6 Hz, 2H), 7.38 (d, J = 8.6 Hz, 2H), 6.17 (s, 1H), 5.17 (d, J = 8.2 Hz, 1H), 4.42 – 4.37 (m, 1H), 3.24 (dd, J = 14.8, 6.8 Hz, 1H), 3.08 (dd, J = 14.8, 7.2 Hz, 1H), 2.76 (d, J = 4.8 Hz, 3H), 1.38 (s, 9H). ^{13}C NMR (100 MHz, $CDCl_3$) δ 171.24, 155.55, 147.12, 144.90, 130.37, 123.81, 80.71, 55.49, 38.64, 28.34, 26.37. LR-MS (MALDI-TOF) *m/z*: cacld for $[C_{15}H_{21}N_3O_5 + Na]^+$ 346.1, found 346.2.

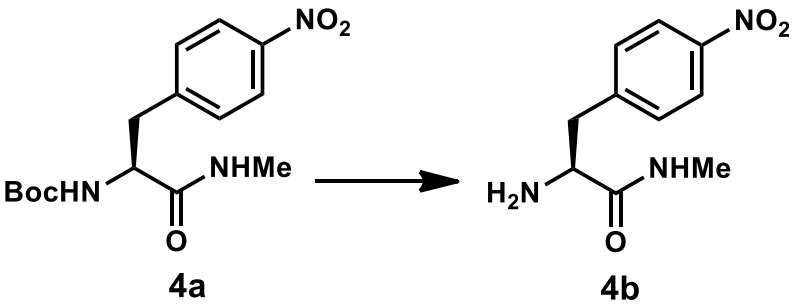

Conditions: TFA, DCM, r.t., 5 h

Compound 4b: A solution of **4a** (480 mg, 1.49 mmol) in DCM (30 mL) was stirred with TFA (20 mL) at room temperature for 6 h. Evaporation of the reaction mixture afforded the product **4b** as a white solid. Yield: 423 mg, 90%. ^{1}H NMR (400 MHz, CD_3OD) δ 8.22 – 8.19 (m, 2H), 7.48 – 7.45 (m, 2H), 4.03 (t, J = 7.4 Hz, 1H), 3.26 – 3.13 (m, 2H), 2.68 (s, 3H). ^{13}C NMR (100 MHz, CD_3OD) δ 169.51, 148.98, 143.47, 131.74, 124.92, 55.33, 38.18, 26.28. LR-MS (MALDI-TOF) *m/z*: cacld for $[C_{10}H_{13}N_3O_3 + Na]^+$ 246.1, found 246.1.

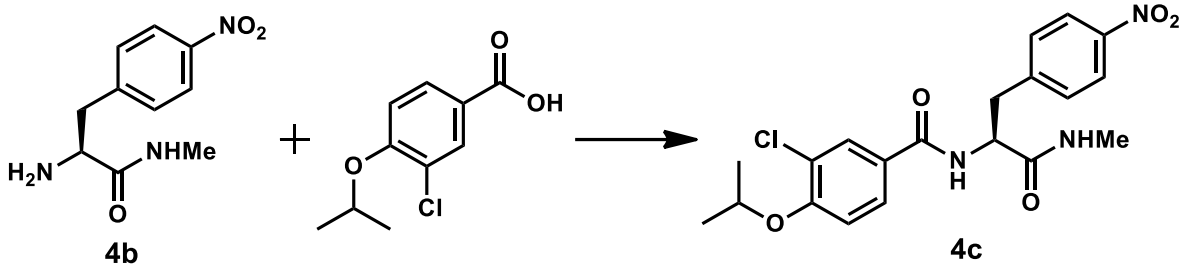

Conditions: HOBT·H_2O, HBTU, DIPEA, DMF, r.t., 17 h

Compound 4c: To a solution of **4b** (406 mg, 1.82 mmol, 1.0 eqv.), 3-chloro-4-isopropoxybenzoic acid[24] (469 mg, 2.18 mmol, 1.2 eqv.), HOBT·H_2O (334 mg, 2.18 mmol, 1.2 eqv.), and HBTU (827 mg, 2.18 mmol, 1.2 eqv.) in DMF (50 mL) was added DIPEA (951 µL, 5.56 mmol, 3.0 eqv.). The reaction mixture was stirred at room temperature for 17 h. It was extracted with EtOAc (35 mL) and sat. $NaHCO_3$aq (100

mL x 3) and washed with brine (100 mL x 3). It was dried over $MgSO_4$, filtered and evaporated *in vacuo.* The crude mixture was purified by column chromatography (SiO_2, EtOAc : hexane = 3:1) to afford the product **4c** as an white solid. Yield: 266 mg, 35%. ^{1}H NMR (400 MHz, $CDCl_3$) δ 8.19 – 8.15 (m, 2H), 7.78 (d, J = 2.3 Hz, 1H), 7.58 (dd, J = 8.6, 2.3 Hz, 1H), 7.43 – 7.41 (m, 2H), 6.93 (d, J = 8.8 Hz, 1H), 6.74 (d, J = 7.9 Hz, 1H), 5.90 (s, 1H), 4.85 – 4.79 (m, 1H), 4.69 – 4.60 (m, 1H), 3.34 – 3.22 (m, 2H), 2.78 (d, J = 4.9 Hz, 3H), 1.41 (d, J = 6.1 Hz, 6H). ^{13}C NMR (100 MHz, $CDCl_3$) δ 171.22, 166.04, 156.86, 147.20, 144.66, 130.36, 129.72, 126.89, 125.79, 124.16, 123.89, 114.04, 72.17, 54.70, 38.47, 26.44, 22.00. LR-MS (MALDI-TOF) *m/z*: cacld for $[C_{20}H_{22}ClN_3O_5 + Na]^+$ 442.1, found 442.1.

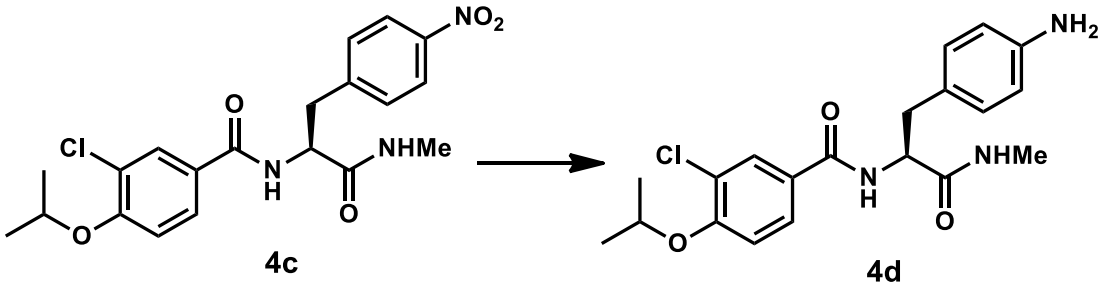

Conditions: Pd/C, H_2 (gas), MeOH, r.t., 2 h

Compound 4d: A solution of **4c** (258 mg, 0.61 mmol) in methanol (10 mL) was stirred with 10% Pd/C (37 mg) catalyst under hydrogen atmosphere at room temperature for 2 h. The reaction mixture filtered through celite and concentrated *in vacuo.* The crude solid was purified by column chromatography (SiO_2, EtOAc : hexane = 10:1) to afford a white solid **4d**. Yield: 112 mg, 47%. ^{1}H NMR (400 MHz, $CDCl_3$) δ 7.78 (d, J = 2.2 Hz, 1H), 7.59 (dd, J = 8.8, 2.2 Hz, 1H), 7.03 (d, J = 8.3 Hz, 2H), 6.95 – 6.85 (m, 2H), 6.63 (d, J = 8.3 Hz, 2H), 5.96 (s, 1H), 4.74 – 4.57 (m, 2H), 3.13 (dd, J = 13.7, 5.8 Hz, 1H), 2.96 (dd, J = 12.8, 8.2 Hz, 1H), 2.72 (d, J = 4.8 Hz, 3H), 1.44 – 1.32 (m, 6H). ^{13}C NMR

(100 MHz, $CDCl_3$) δ 171.79, 165.71, 156.54, 145.38, 130.32, 129.74, 129.03, 126.89, 126.62, 124.06, 115.57, 114.17, 72.11, 55.49, 38.08, 26.34, 22.02. LR-MS (MALDI-TOF) *m/z*: cacld for $[C_{20}H_{24}ClN_3O_3 + Na]^+$ 412.1, found 412.1.

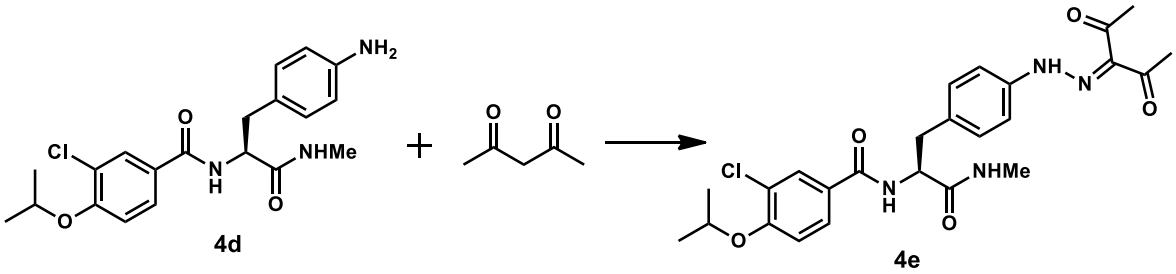

Conditions: (a) $NaNO_2$, H_2O, AcOH, HCl, 0 ^oC, 1 h, (b) NaOAc, EtOH, H_2O, r.t., 1 h

Compound 4e: 115 µL aqueous solution of $NaNO_2$ (27 mg, 0.40 mmol, 1.2 eq.) was added to a solution of **4d** (110 mg, 0.33 mmol, 1.0 eq.) in AcOH (450 µL) and 12 M HCl (75 µL) at 0 °C. The resulting solution was stirred at 0 °C for 1 hour and transferred to a suspension of pentan-2,4-dione (45 µL, 0.43 mmol, 1.3 eq.) and NaOAc (82 mg, 0.99 mmol, 3 eq.) in EtOH (315 µL) and H_2O (174 µL), forming a yellow precipitate. The reaction mixture was stirred for 1 hour at room temperature and the precipitate was collected by filtration, washed with H_2O, H_2O : EtOH = 1 :1, and hexane. It was dried *in vacuo* to afford a yellow solid **4e**. Yield: 76 mg, 46%. ^1H NMR (400 MHz, $CDCl_3$) δ 7.78 (d, *J* = 2.3 Hz, 1H), 7.60 (dd, *J* = 8.6, 2.3 Hz, 1H), 7.37 – 7.28 (m, 5H), 6.93 (d, *J* = 8.9 Hz, 1H), 6.74 (d, *J* = 7.8 Hz, 1H), 5.81 – 5.77 (m, 1H), 4.79 – 4.72 (m, 1H), 4.67 – 4.60 (m, 1H), 3.23 – 3.12 (m, 2H), 2.78 – 2.76 (m, 3H), 2.60 (s, 3H), 2.48 (s, 3H), 1.41 – 1.34 (m, 6H). ^{13}C NMR (100 MHz, $CDCl_3$) δ 198.15, 197.21, 171.27, 165.76, 156.74, 140.74, 134.56, 133.38, 130.74, 129.69, 126.87, 126.31, 124.19, 116.65, 114.18, 72.17, 55.11, 38.31, 31.83, 26.80, 26.45, 22.03. LR-MS (MALDI-TOF) *m/z*: cacld for $[C_{25}H_{29}ClN_4O_5 + Na]^+$ 523.2, found 523.1.

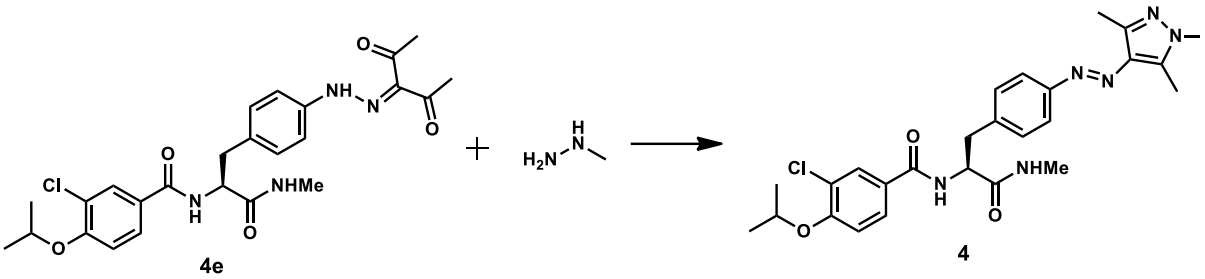

Conditions: EtOH, 80 ºC, 3 h

Compound 4: Methylhydrazine (8.25 µL, 0.16 mmol, 1.0 eq.) was added to a solution of **4e** (76 mg, 0.16 mmol, 1.0 eq.) in EtOH (10 mL) and refluxed for 3 hours. After evaporation, the residual crude solid was purified using reverse-phase HPLC with a mobile phase gradient (acetonitrile / water with 0.1% TFA = 40 to 100% of acetonitrile in water for 81 min) to afford **4** as an orange solid. Yield: 45 mg, 55%. ^{1}H NMR (400 MHz, $CDCl_3$) δ 7.80 (d, J = 2.3 Hz, 1H), 7.75 – 7.73 (m, 2H), 7.61 (dd, J = 8.6, 2.3 Hz, 1H), 7.35 (d, J = 8.4 Hz, 2H), 7.01 (d, J = 7.9 Hz, 1H), 6.93 (d, J = 8.9 Hz, 1H), 5.97 (d, J = 4.9 Hz, 1H), 4.85 – 4.79 (m, 1H), 4.67 – 4.61 (m, 1H), 3.84 (s, 3H), 3.27 (dd, J = 14.8, J = 6.2 Hz, 1H), 3.17 (dd, J = 12.8, J = 8.2 Hz, 1H), 2.76 (d, J = 4.8 Hz, 3H), 2.59 (s, 3H), 2.52 (s, 3H), 1.40 (d, J = 6.1 Hz, 6H). ^{13}C NMR (100 MHz, $CDCl_3$) δ 171.94, 166.13, 156.82, 152.53, 142.42, 139.27, 138.52, 134.87, 130.03, 129.86, 126.95, 126.00, 124.19, 122.38, 114.13, 72.15, 55.30, 38.53, 35.68, 26.53, 22.00, 13.20, 10.03. HR-MS (ESI) *m/z*: calcd for $[C_{26}H_{31}ClN_6O_3 + Na]^+$ 533.20438, found 533.20392.

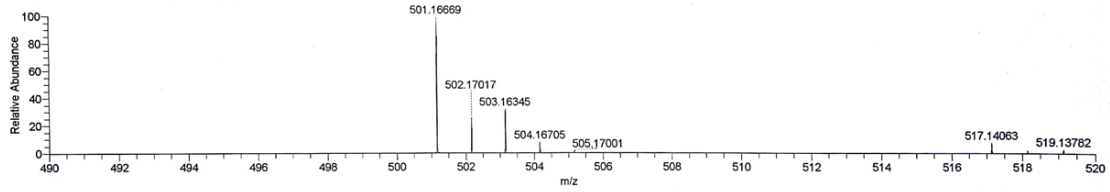

Figure 2-9. HR-MS (ESI) mass spectrum of Cenp-E inhibitor **1**: *m/z* = 501.16669 $[C_{26}H_{27}ClN_4O_3 + Na]^+$ (calculated mass for the most abundant isotope: 501.16693)

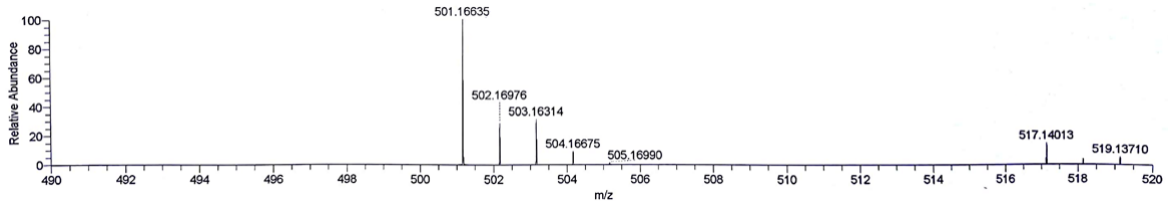

Figure 2-10. HR-MS (ESI) mass spectrum of Cenp-E inhibitor **2**: *m/z* = 501.16635 $[C_{26}H_{27}ClN_4O_3 + Na]^+$ (calculated mass for the most abundant isotope: 501.16693)

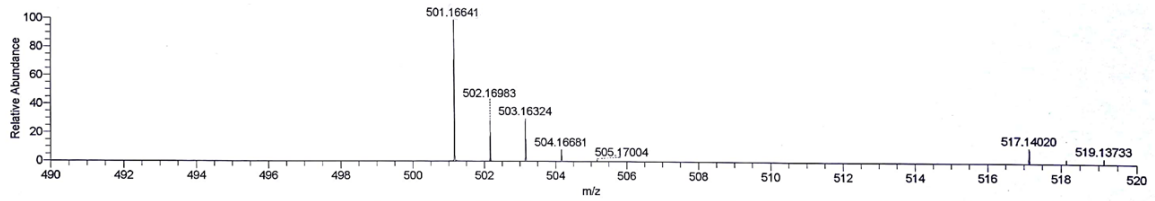

Figure 2-11. HR-MS (ESI) mass spectrum of Cenp-E inhibitor **3**: *m/z* = 501.16641 $[C_{26}H_{27}ClN_4O_3 + Na]^+$ (calculated mass for the most abundant isotope: 501.16693)

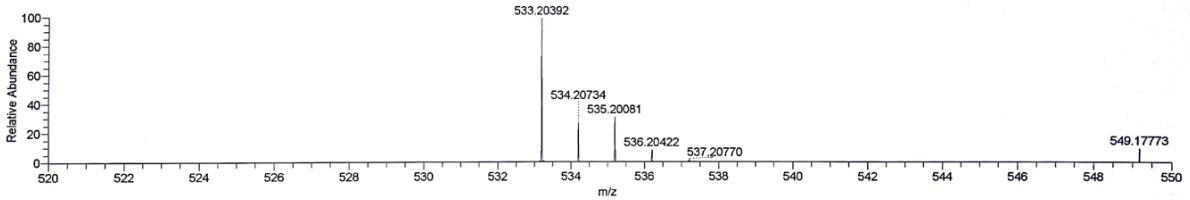

Figure 2-12. HR-MS (ESI) mass spectrum of Cenp-E inhibitor **4**: *m/z* = 533.20392 $[C_{26}H_{31}ClN_6O_3 + Na]^+$ (calculated mass for the most abundant isotope: 533.20438)

2.6. References

(1) Scholey, J. M.; Brust-Mascher, I.; Mogilner, A. Cell Division, *Nature* **2003**, *422*, 746–752.

(2) Cleveland, D.; W., Mao, Y.; Sullivan, K. F. Centromeres and Kinetochores: from Epigenetics to Mitotic Checkpoint Signaling. *Cell* **2003**,*112*, 407–421.

(3) Maiato, H.; Gomes, A. M.; Sousa, F.; Barisic, M. Mechanisms of Chromosome Congression during Mitosis, *Biology* **2017**, *6*, 13.

(4) Barisic, M.; Aguiar, P.; Geley, S.; Maiato, H. Kinetochore Motors Drive Congression of Peripheral Polar Chromosomes by Overcoming Random Arm-ejection Forces. *Nat. Cell Biol*. **2014**, *16*, 1249–1256.

(5) Skibbens, R. V.; Rieder, C. L.; Salmon, E. D. Kinetochore Motility after Severing Between Sister Centromeres Using Laser Microsurgery: Evidence that Kinetochore Directional Instability and Position is Regulated by Tension. *J. Cell Sci.* **1995**, *108*, 2537–2548.

(6) Brouhard, G. J.; Hunt, A. J. Microtubule Movements on the Arms of Mitotic Chromosomes: Polar Ejection Forces Quantified in Vitro. *Proc. Natl. Acad. Sci. USA* **2005**, *102*, 13903–13908.

(7) Lampson, M. A.; Kapoor, T. M. Unraveling Cell Division Mechanisms with Small-Molecule Inhibitors. *Nat. Chem. Biol*. **2006**, *2*, 19–27.

(8) Garcia-Saez, I.; Yen, T.; Wade, R. H.; Kozielsk, F. Crystal Structure of the Motor Domain of the Human Kinetochore Protein CENP-E. *J. Mol. Biol.* **2004,** *340,* 1107-1116.

(9) Wood, K. W.; Sakowicz, R.; Goldstein, L. S.; Cleveland, D. W. CENP-E is a Plus End-directed Kinetochore Motor Required for Metaphase Chromosome Alignment. *Cell* **1997**, *91*, 357–366.

(10) Kim, Y.; Heuser, J. E.; Waterman, C. M.; Cleveland, D. W. CENP-E Combines a Slow, Processive Motor and a Flexible Coiled Coil to Produce an Essential Motile Kinetochore Tether. *J. Cell Biol*. **2008**, *181*, 411–419.

(11) McEwen, B.F.; Chan, G.K.; Zubrowski, B.; Savoian, M.S.; Sauer, M.T.; Yen, T.J. CENP-E is Essential for Reliable Bioriented Spindle Attachment, but Chromosome Alignment can be Achieved via Redundant Mechanisms in Mammalian Cells. *Mol. Biol. Cell* **2001**, *12*, 2776–2789.

(12) Yen, T.J.; Compton, D.A.; Wise, D.; Zinkowski, R.P.; Brinkley, B.R.; Earnshaw, W.C.; Cleveland, D.W. CENP-E, a Novel Human Centromere-Associated Protein Required for Progression from Metaphase to Anaphase. *EMBO J.* **1991**, *10*, 1245–1254.

(13) Yao, X.; Abrieu, A.; Zheng, Y.; Sullivan, K.F.; Cleveland, D.W. CENP-E Forms a Link Between Attachment of Spindle Microtubules to Kinetochores and the Mitotic Checkpoint. *Nat. Cell Biol.* **2000**, *2*, 484–491.

(14) Borowiak, M.; Nahaboo, W.; Reynders, M.; Nekolla, K.; Jalinot, P.; Hasserodt, J.; Rehberg, M. Delattre, M.; Zahler, S.; Vollmar, A.; Trauner, D.; Thorn-Seshold, O. Photoswitchable Inhibitors of Microtubule Dynamics Optically Control Mitosis and Cell Death. *Cell* **2015**, *162*, 403–411.

(15) Zhang, H.; Aonbangkhen, C.; Tarasovetc, E. V.; Ballister, E. R.; Chenoweth, D. M.; Lampson, M. A. Optogenetic Control of Kinetochore Function. *Nat. Chem. Biol.* **2017**, *13*, 1096–1101.

(16) El-Arabey A.A.; Salama S.A.; Abd-Allah A.R.; CENP-E as a Target for Cancer Therapy: Where Are We Now? *Life Sciences* **2018**, *208*, 192–200.

(17) Wood, K.W.; Lad, L.; Luo, L.; Qian, X.; Knight, S.D.; Nevins, N.; Brejc, K.; Sutton, D.; Gilmartin, A.G.; Chua, P.R.; et al. Antitumor Activity of an Allosteric Inhibitor

of Centromere-associated Protein-E. *Proc. Natl. Acad. Sci. USA* **2010**, *107*, 5839–5844.

(18) Ding, X.; Yan, F.; Yao, P.; Yang, Z.; Wan, W.; Wang, X.; Liu, J.; Gao, X.; Abrieu, A.; Zhu, T.; et al. Probing CENP-E Function in Chromosome Dynamics Using Small Molecule Inhibitor Syntelin. *Cell Res.* **2010**, *20*,1386–1389.

(19) Kung, P.-P.; Martinez, R.; Zhu, Z.; Zager, M.; Blasina, A.; Rymer, I.; Hallin, J.; Xu, M.; Carroll, C.; Chionis, J.; et al. Chemogenetic Evaluation of the Mitotic Kinesin CENP-E Reveals a Critical Role in Triple-negative Breast Cancer. *Mol. Cancer Ther.* **2014**, *13*, 2104–2115.

(20) Ohashi, A.; Ohori, M.; Iwai, K.; Nambu, T.; Miyamoto, M.; Kawamoto, T.; Okaniwa, M. A Novel Time-Dependent CENP-E Inhibitor with Potent Antitumor Activity. *PLoS ONE* **2015**, *10*, e0144675.

(21) Szymanski, W.; Beierle, J. M.; Kistemaker, H. A. V.; Velema, W. A.; Feringa, B. L. Reversible Photocontrol of Biological Systems by the Incorporation of Molecular Photoswitches *Chem. Rev*. **2013**, *113*, 6114-6178.

(22) Qian, X.; McDonald, A.; Zhou, H.-J.; Adams, N. D.; Parrish, C.A.; Duffy, K. J.; Fitch, D. M.; Tedesco, R.; Ashcraft, L. W.; Yao, B.; et al. Discovery of the First Potent and Selective Inhibitor of Centromere-Associated Protein E: GSK923295. *ACS Med. Chem. Lett.* **2010**, *1*, 30–34.

(23) Gudimchuk, N.; Vitre, B.; Kim, Y.; Kiyatkin, A.; Cleveland, D.W.; Ataullakhanov, F. I.; Grishchuk, E. L. Kinetochore Kinesin CENP-E is a Processive Bi-directional Tracker of Dynamic Microtubule Tips. *Nat. Cell Biol.* **2013**, *15*, 1079–1088.

(24) Skidmore, J.; Heer, J.; Johnson, C. N.; Norton, D.; Redshaw, S.; Sweeting, J.; Hurst, D.; Cridland, A.; Vesey, D.; Wall, I.; Ahmed, M.; Rivers, D.; Myatt, J.; Giblin, G.; Philpott, K.; Kumar, U.; Stevens, A.; Bit, R. A.; Haynes, A.; Taylor, S.; Watson,

R.; Witherington, J.; Demont, E. and. Heightman, T. D. Optimization of Sphingosine-1-phosphate-1 Receptor Agonists: Effects of Acidic, Basic, and Zwitterionic Chemotypes on Pharmacokinetic and Pharmacodynamic Profiles, *J. Med. Chem.* 57, 24, 10424-10442.

Chapter 3

Molecular Crankshaft Effect Converting Piston-like Molecular Motion to Continuous Rotation of Macro Objects

3.1 Introduction

In the living organism, motor proteins such as myosin, kinesin, and dynein are functioning as molecular machines which can continuously convert the chemical energy stored in adenosine 5′-triphosphate to mechanical work of muscle, motion of flagella, and transport of micro-objects in cells.[1] While there are several definitions of “molecular machine”, it is defined as molecules transforming continuously some energy to mechanical work for outside world by a molecular level mechanism in a narrow sense.[2] The studies aiming at the synthesis of artificial molecular machines are one of the most challenging fields. Many efforts are made to mimic the motion of machines of the real world such as shuttles,[3,4] elevators,[5] piston,[6] nanocar,[7] plier,[8] and so on with synthesized molecules. In these systems, molecules detect external stimuli, such as light, electric field, pH, solvent polarity, ion, or temperature, and then change their physical properties reversibly accompanying a molecular motion: switching between two states or piston-like movement between two positions. However, these molecular machines are not suited in strict manner for the ones defined above. In fact, the molecules just detect some energy as stimuli and change their states reversibly accompanying a molecular or macroscopic motion, without converting energy to work for outside world repeatedly. These types of systems come under the category of piston action or switch, from which we cannot generate continuous work.

In the real world, engines transform the energy of fuel to the work by combustion where crankshaft motion is utilized for the piston action of a cylinder undergoing a continuous rotational motion with an axis. To realize a true molecular machine transforming energy to work continuously, I need to create a crankshaft contrivance functioning in the molecular level. Furthermore, a strategy to assemble the motion of each molecule into the same direction is desired for extracting the energy

transformation as a visible macroscopic motion. In 2006, Feringa and colleagues succeeded in the directional rotation of a glass rod of several tens micrometer size located on a liquid crystalline (LC) film as the result of the rotational reorganization of polygonal fingerprint texture of the cholesteric LC (CLC) induced by *trans*−*cis* photoisomerization of an embedded chiral ethylene derivative.[9−11] Although this molecular system seems to be one of the examples of molecular machines transforming light energy to work, I need to categorize it to a “switch” not to a machine because they could not unidirectionally rotate the glass rod with the continuous manner. The rotational motion stops at the *cis*-rich photostationary state and the reverse rotational motion to the opposite direction was obtained upon thermal *cis* to *trans* isomerization. A continuous and unidirectional rotational motion of LC pattern has been demonstrated with CLC films by using the change of molecular orientation under light irradiation or unidirectional permeation of water molecules.[12,13] However, it is not clear whether this system can perform macroscopic mechanical work or not by using these orientational changes of molecules in CLC films. Ikeda[14] and Yu[15] have already succeeded in demonstrating the directional rotation or linear translocation of films by using a photochromic LC polymer. In these systems, however, the directionality of the rotational or linear movement of films caused by the photoinduced extension and contraction of the film is originated from the mechanism not at the molecular level but at the macroscopic level: the direction of the movement of the films is determined by the positions irradiated with UV or visible lights on the film.

I have already explored LC systems similar to the Feringa’s with novel chiral azobenzene[16−18] and helicene[19] derivatives, usually exhibiting rotary motions of glass rods on thin CLC films in opposite directions upon UV and visible light. I showed the reversible rotation in relatively thin CLC films based on dibromo-substituted

azobenzophane (Figure 3-1a).[16] During this study, I found an unusual phenomenon that the photoinduced LC texture transition is totally different compared with that of previous study. In a thick CLC film condition, the emergence of a new texture was observed during the photoisomerization of chiral azobenzene from *cis* to *trans* form. By manipulating this unusual phenomenon, herein I demonstrate the first example of the molecular crankshaft effect displaying accumulative unidirectional rotation of macroscopic glass flakes on the surface of chiral-azobenzene doped CLC films under light irradiation. *Trans*−*cis* isomerization upon UV irradiation causes the rotation of glass flakes, whereas *cis*−*trans* isomerization upon irradiation with visible light results in a paused state, instead of reverse rotation. It implies that the ultimate work would not be zero, which intrinsically improved the system from previous demonstrations.

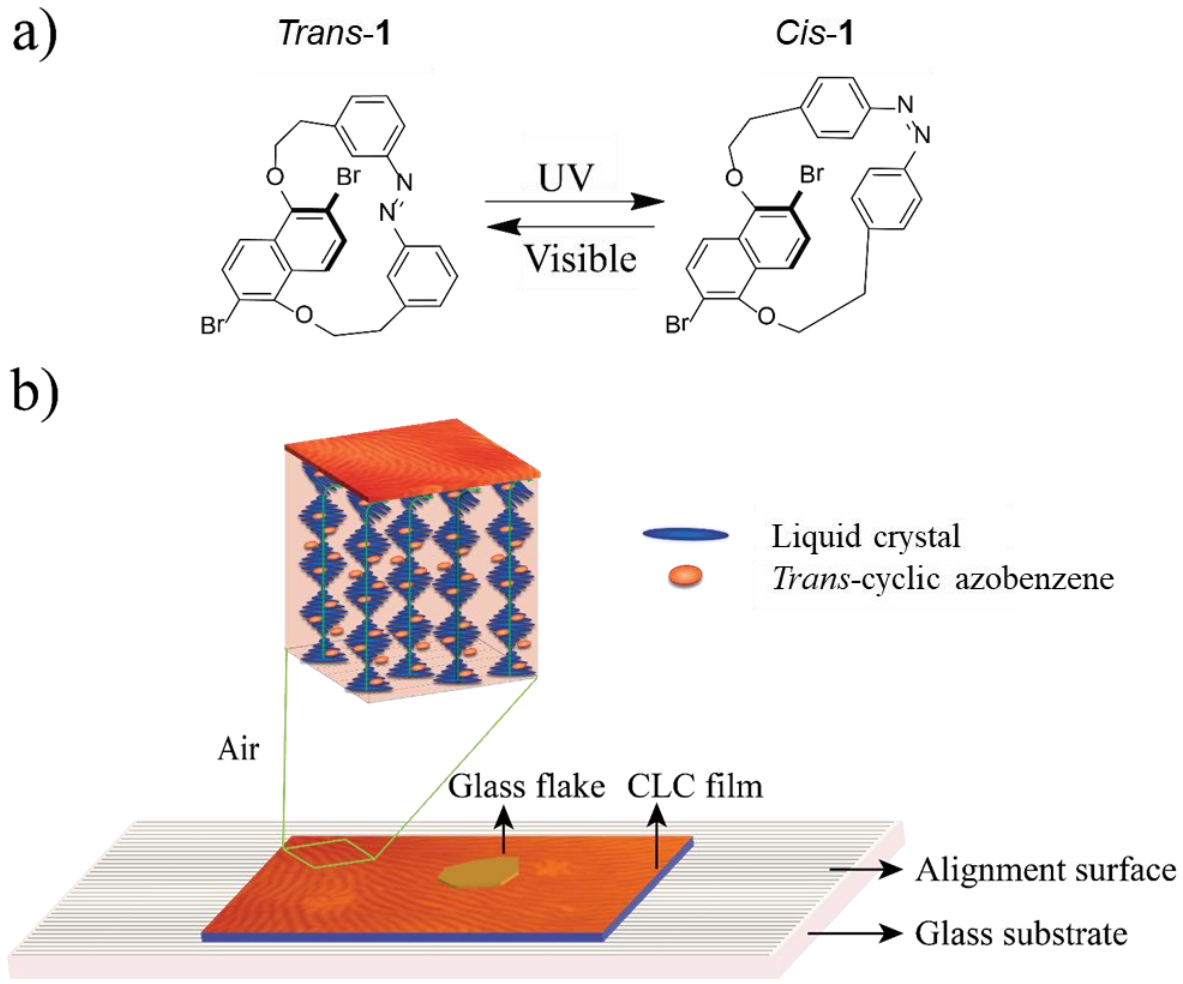

Figure 3-1. a) Molecular structure and photoisomerization of cyclic azobenzene based motor **1**. b) Schematic representation of formation of CLC film on the rubbed polyimide surface and sprinkle of the glass flakes on the open surface of the film to get rotational work.

3.2 Results and Discussion

3.2.1 Photoinduced Unidirectional and Continuous Mechanical Work

In the present system, dibromo-substituted azobenzophane at 1 wt % was dissolved into nematic LC host ZLI-1132, and the resultant continuous polygonal fingerprint texture was formed on glass slides pretreated with an unidirectionally rubbed polyimide alignment layer (Figure 3-1b). The reorganization of the polygonal

fingerprint texture of ca. 52 μm thick CLC films was monitored under UV and visible light irradiation with a polarizing optical microscope (POM) as shown in Figure 3-2. Under UV (366 nm) light irradiation, the fingerprint texture showed homogeneous rotational reorganization with an expansion of the line gaps as evidenced from Figure 3-2a−c which is ascribed to the lengthening of helical pitch associated with the increasing concentration of bent shaped *cis* isomer of lower helical twisting power (HTP) in CLC film. [20−22] Change of the HTP of **1** in nematic host ZLI-1132 before and after light irradiation has already been reported: by the UV light irradiation, initial HTP −35 μm^{-1} decreased to −18 μm^{-1} at PSS_{366nm}.[16] On the other hand, the abnormal texture transformation was observed during *cis*−*trans* photoisomerization under visible light (436 nm) irradiation (30 mW cm^{-2}) that is instead of typically observed fingerprint texture rotation to the opposite direction (Figure 3-2d,e). By a careful comparison of the round-shaped-patterns with 10−30 μm size in diameter with the ever-known textures for CLC film, I could assign it as a kind of focal conic textures where numerous small domains with different sizes and shapes were formed. Usually, focal conic texture comprises independent multiple domains with intrinsic helical pitch, but the helical axis of each domain is randomly oriented throughout the surface. This type of texture is also found in the cuticle of Plusiotis gloriosa in nature[23] and CLC films upon electric field application[24,25] and also upon photoisomerization of a doped azobenzene derivative.[26,27] Continuous visible light irradiation or thermal back process resulted in merging of scattered small-domain boundaries, leading to the formation of large domains. Simultaneously, the fingerprint texture emerged in several domains (Figure 3-2e) and finally merged recovering the initial polygonal fingerprint texture (Figure 3-2f) and HTP of motor **1** recovered to −33 μm^{-1} at PSS_{436nm}.[16] The reappeared fingerprint texture did not show any rotational reorganization of the lines with further

visible light irradiation. I also observed that the formation of the focal conic texture highly relies on the film thickness and irradiation intensity of visible light. By increasing the film thickness, it had a stronger tendency to form focal conic domains accompanying longer time to recover the initial fingerprint texture. Exposure to 436 nm light source with 6% of it's original intensity (1.8 mW cm^{-2}) showed no focal conic texture, regardless of the film thickness, while that with 25% of original intensity (7.5 mW cm^{-2}) resulted in the mixed domains of polygonal fingerprint and focal conic textures.

To realize the rotational behavior of micro-objects generated by the rotation of photoinduced polygonal fingerprint texture, glass flakes were sprinkled on the surface of film followed by the photoirradiation with light of wavelength 366 and 436 nm. Figure 3-2 shows a series of two cycles of rotation and standstill state of a glass flake on the surface of CLC film under subsequent UV and visible light irradiation. According to the chiral nature of the embedded molecule **1**,[28] the texture and glass flakes were rotated in either a clockwise (doped with S- (−)-*E*-**1**) or a counterclockwise (doped with R-(−)-*E*-**1**) fashion. Under UV irradiation, a glass flake on the surface of the CLC film (S-(−)-*E*-**1** doped in ZLI-1132) has executed rotation in the clockwise direction as the result of rotational reorganization of the fingerprint texture, and rotation continued until reaching the photostationary state (PSS_{366nm}, Figure 3-2b,c,g,h). During this irradiation, the glass flake made approximately four and a half full turn with 3°/s rotation speed. The rotation speed of the glass flakes increased by raising the UV light intensity, which is consistent with our previous observation with the thin CLC films[16] but has no flake size dependence, because it is governed by the rotational speed of the polygonal fingerprint texture. After PSS_{366nm}, irradiation of the film with visible light changed the

fingerprint texture to focal conic patterns, resulting in the standstill state of the glass flake instead of reverse rotation (Figure 3-2-d,e,i).

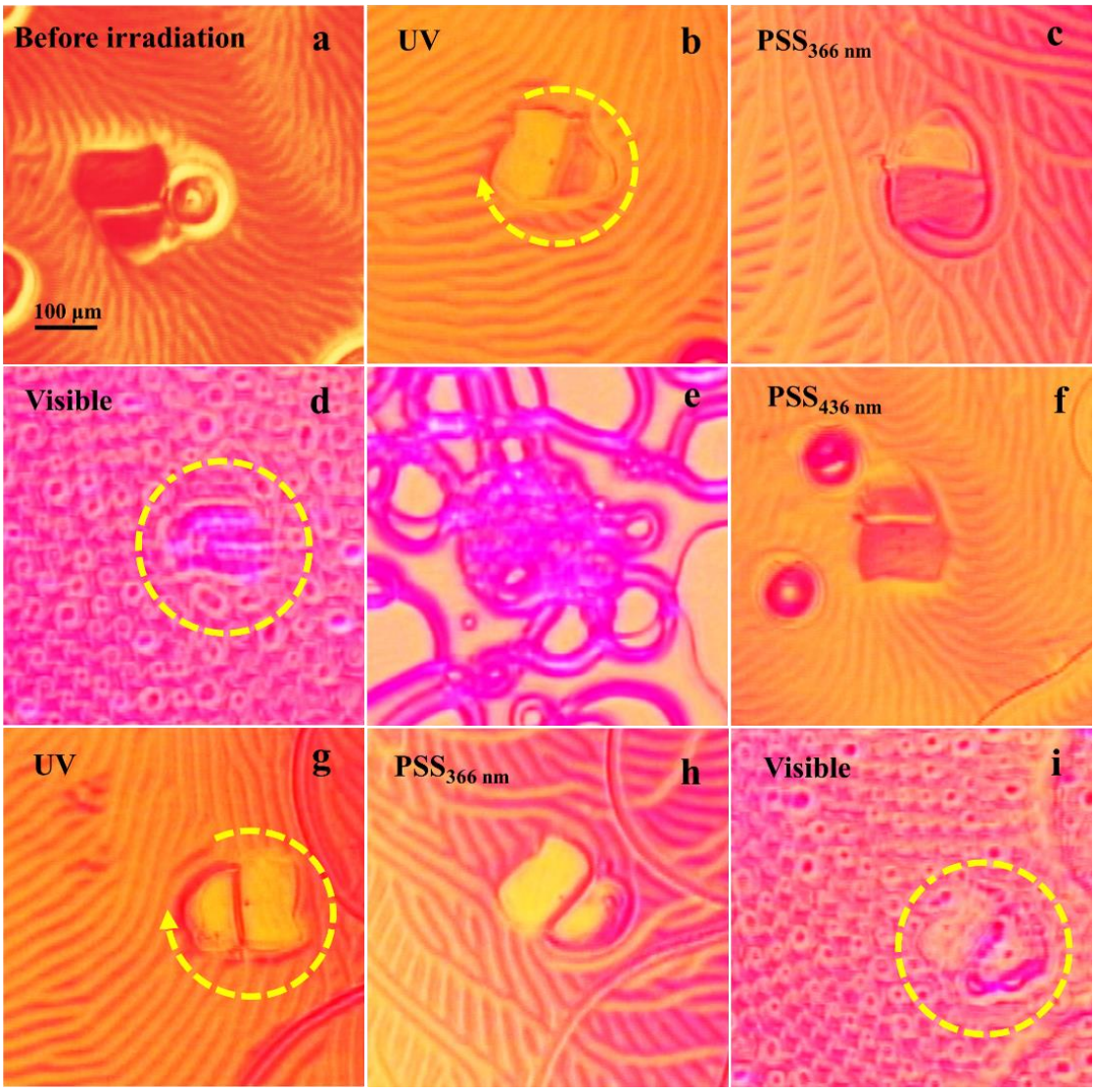

Figure 3-2. Photoinduced polygonal fingerprint texture change for 3 cycles under alternative UV and visible light irradiation, resulting several full turns of unidirectional rotation of glass flakes on the surface of a CLC film (1 wt% of S-(-)-*E*-**1** in ZLI-1132). Clockwise rotation of glass flake (b→c and g→h) upon irradiation with UV light (366 nm). Immobile glass flake (d→f and i) upon irradiation with visible light (436 nm with

30 mWcm^{-2} intensity). During the depicted process, the flake made approximately four and half full turns.

Alternating UV and visible light irradiation produced multicycle unidirectional rotation of glass flakes, and the rotation angle through the sequences was examined as shown in Figure 3-3. The steady (red line) and steeper slope (black line) of the plot indicates the pause and rotation movement of glass flakes, respectively. In each UV light irradiation (*trans*−*cis* isomerization), glass flakes showed rotation with angles varying from 300° to 500° without any backward rotation upon visible light (*cis*−*trans* isomerization), which led to the accumulation of the rotation angle. After six complete sequences of UV and visible light irradiations, glass flakes performed over 3000° rotation in one direction which has never been achieved so far to the best of our knowledge. It was also confirmed that enantiomers R-(+)-*E*-**1** and S-(−)-*E*-**1** undergo comparable rotation angles with opposite direction of rotation each other. Therefore, this phenomenon satisfies the definition or criteria of real molecular machine implementing a molecular crankshaft effect which can continuously utilize the external energy to perform mechanical work by using the molecular switching mechanism.

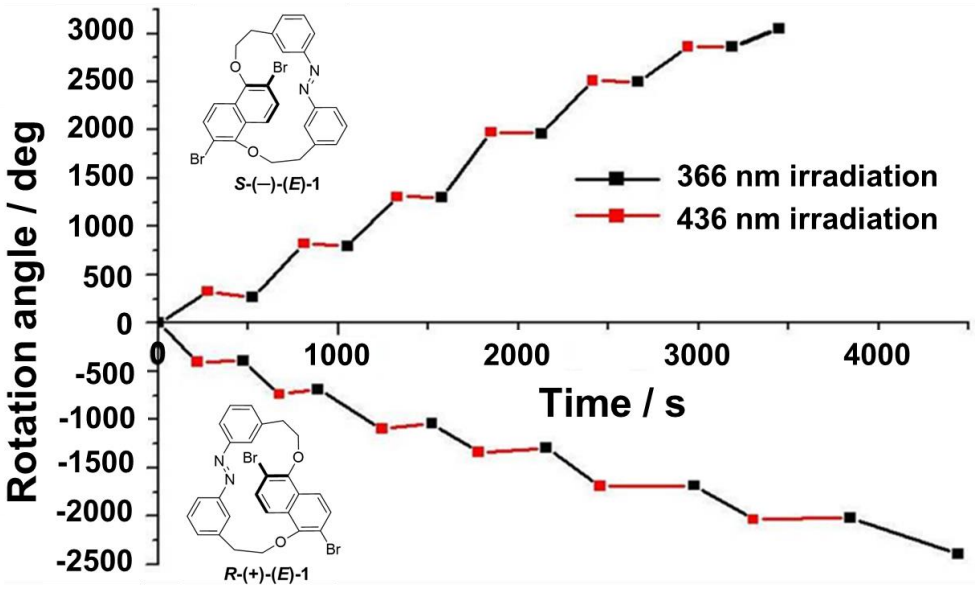

Figure 3-3. Change in rotation angle of glass flakes upon alternating UV (black line) and visible light (red line) irradiation on the surface of cholesteric liquid crystalline films containing *R*-(+)-*E*-**1** and *S*-(-)-*E*-**1** (1 wt%) in ZLI-1132.

3.2.2 Molecular Mechanism of Unidirectional Rotation

To gain the insights into the origin of unusual texture transition by *cis* to *trans* processes in self-assembled superstructures, I tried to further explore the photoisomerization behavior of **1** in a CLC film. Figure 3-4a shows the UV−visible absorption spectra of CLC film with the thickness of ca. 52 μm. Absorption band centered at 336 nm is assigned to π−π* transition of azobenzene moiety. Irradiation with UV light onto the film induces the decrease of the absorption band intensity corresponding to the π−π* transition of the *trans* isomers caused by conversion from the *trans* to *cis* isomer reaching PSS_{366nm}. Subsequent 436 nm light irradiation induces gradual recovery of π−π* absorption band intensity centered at 336 nm and reaching to the PSS_{436nm}. It is noteworthy that only 50% of absorbance at 336 nm was recovered at PSS_{436nm}, though 90% of contained *trans* isomer in the LC film was recovered at PSS_{436nm} which was determined by high-pressure liquid chromatography (HPLC) as shown in Figure 3-4b. The calculated recovery of the absorbance at PSS_{436nm} for 100, 52, and 18 μm thick films were ca. 50% of initial absorbance (Figure 3-4c). In contrast, for the 11 μm thin film, 90% of the absorbance was recovered at PSS_{436nm} which matches to the isomer ratio of 90% *trans* measured by HPLC. Interestingly, the LC texture transition was consistent with the absorption transition behavior. In case of the film of 18 μm or thicker, a stable focal conic texture was observed during the 436 nm irradiation. Moreover, thin CLC films (ca. 11 μm) never showed a focal conic texture, and the polygonal fingerprint texture could reversibly rotate under alternating UV and visible light irradiation.

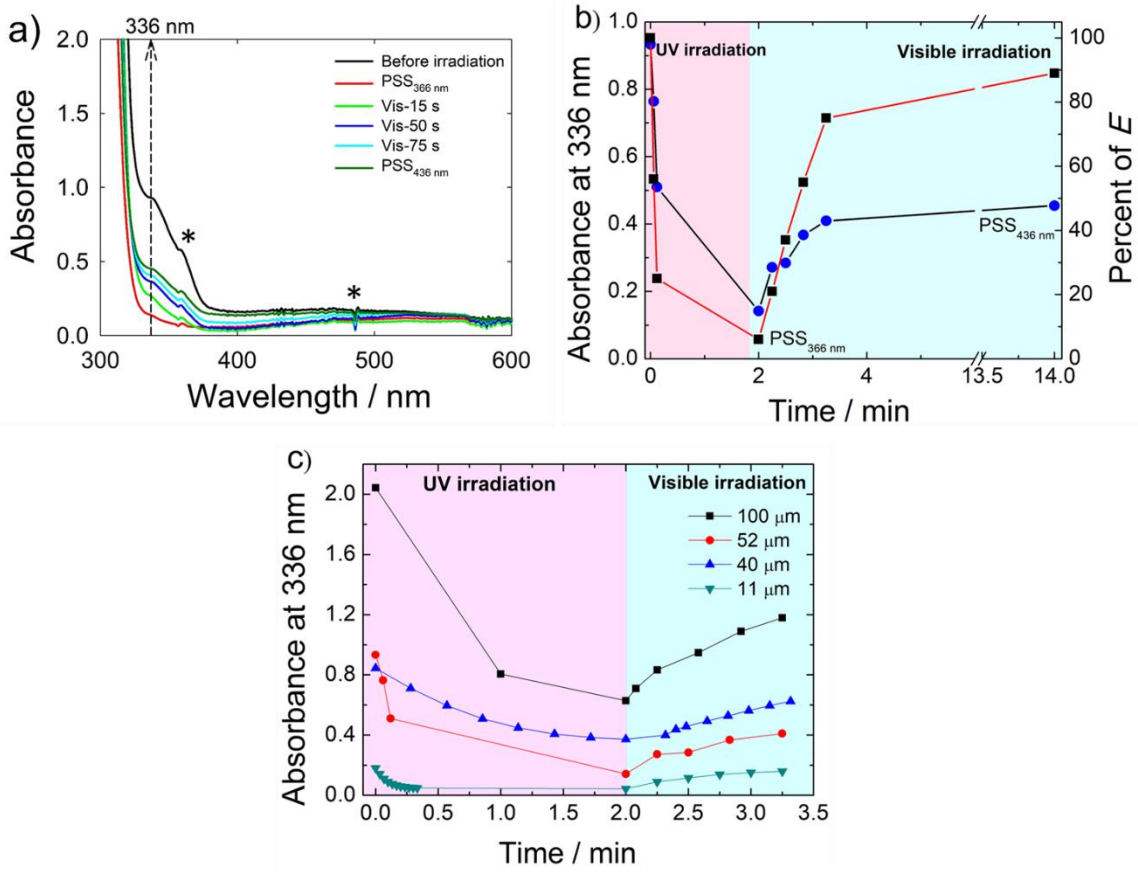

Figure 3-4. (a) UV−visible absorption spectra of a 52 μm thick CLC film doped with **1** (1 wt % of S-(−)-*E*-**1** in ZLI-1132) upon light irradiation with different wavelengths, (b) change of the absorbance and percent of *trans* isomer in the film (52 μm) under UV and visible light irradiation. Red line, black square; percent of *trans* isomer and black line, blue circle; absorbance change monitored at 336 nm. (c) Absorbance change of CLC films with different film thickness upon UV and visible light irradiation; black line (100 μm), red line (52 μm), blue line (18 μm), green line (11 μm). (Spikes in the spectra at around 365 and 486 nm pointed with the mark "*" are noises coming from the spectrometer.)

In case of CLC films, the absorbance of the azobenzene derivatives is depending on not only the isomer ratio but also the orientation of molecules.[27] Basically, when the directions of π−π* transition moment of azobenzene and the

electric field of the incident light are parallel to each other, molecules show the maximum absorbance. If molecules become tilted from their parallel position, they cannot effectively absorb the light resulting in decrease of the absorption. It is generally known that CLC film showing a polygonal fingerprint texture has its helical director align parallel to the substrate at the interface of air while perpendicular in the bulk. In addition, rod-like *trans* isomer of azobenzene is mesogenic and which is likely to orient parallel to the long axis of LC host molecules and it determines the formation and order of LC molecules in domains. Isomerization of doped *E*-azobenzene molecules plays a crucial role for the reorganization of the polygonal fingerprint texture of the CLC film. Upon UV light irradiation on the thick film, *trans*-**1** is converted to the *cis*-**1** and at PSS_{366nm} CLC film maintains the polygonal fingerprint texture with an elongated helical pitch (Figure 3-5a−c). The bent shape of *cis*-**1** molecules has no mesogenic property to affect the helical pitch and the direction of helical axis of the LC molecules, resulting in random orientation of the *cis*-**1** isomers in the film (Figure 3-5c). As soon as irradiating the film at PSS_{366nm} with visible light at 436 nm, the *trans*-**1** isomers suddenly emerged replacing the randomly distributed *cis*-**1** isomers and probably acted as “seed” to induce domains with randomly oriented helices (Figure 3-5d). These randomly oriented domains with many boundaries across the surface of the film result in the focal conic texture which lacks the momentum of rotational reorganization of the LC texture and thereby resulting in the no rotation of the macroscopic object on the film. Then, domains are gradually reorganized again by the continuous visible light irradiation to form a homogeneous and original fingerprint texture which can induce rotational motion again upon *trans* to *cis* isomerization of **1**. Contrary to the thick film (>18 μm), the thin film (11 μm) did not show the formation of a focal conic texture even during the visible light irradiation. When average thickness

of the LC film is thinner than the size of the focal conic domain, the texture can be governed by the alignment layer of the substrate. As described above, the well-controlled cholesteric textures accompanied with unidirectional rotation and the paused state of glass flakes can be compared with a “crankshaft” system in the real world. The *trans*−*cis* isomerization of the azobenzene unit is successfully utilized for the continuous unidirectional rotation of the microsized object, while the second process (*cis* to *trans*) results in a paused state (focal conic texture), instead of typical reverse rotation, during the recovery of polygonal fingerprint texture for accumulative unidirectional sequential rotation.

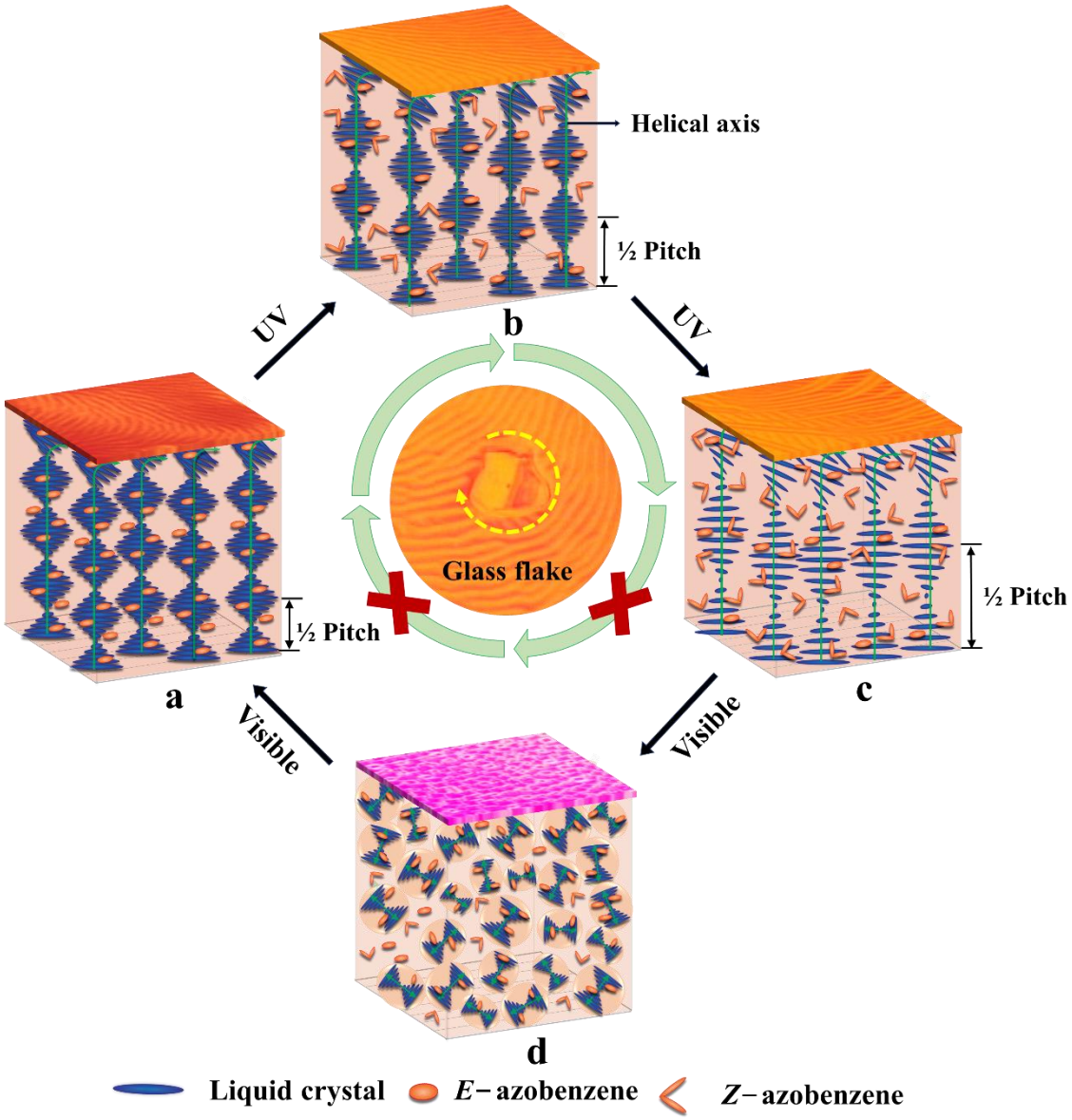

Figure 3-5. Effect of *trans*/*cis* photoisomerization of molecular motor **1** on the texture transition of CLC film under UV and visible light irradiation and consequences to continuous rotation of glass flake.

3.3. Conclusions

I have successfully demonstrated the molecular crankshaft effect that actualizes a continuous conversion of “back and forth” structural changes in a chiral azobenzene induced by light energy to mechanical work, *i.e.* rotation of the glass

flakes. From our observations, it is clear that rotation of the glass flakes on CLC film is governed by the photoisomerization as well as orientation of embedded chiral photoresponsive dopant molecules. Our new findings and the comprehensive analysis with photoresponsive liquid crystal would contribute to develop real molecular machines that are capable of transforming light energy to work.

3.4. Experimental

The nematic liquid crystal ZLI-1132 was gifted by Merck company. The guest molecule, dibromo-substituted azobenzophane **1** was synthesized and characterized using a previously reported procedure from our group.[16] Cholesteric liquid crystal solution was prepared by mixing ZLI-1132 and the dopant **1** (1 wt%) followed by the addition of a few drops of dichloromethane. The solvent was evaporated under reduced pressure and the mixture was introduced on glass slides coated with unidirectionally rubbed polyimide alignment layer and was observed under a polarizing optical microscope. The glass flake REF-160 (thickness, ~5±2 μm, diameter, ~300-150 μm) was purchased from Nippon Sheet Glass Co. Ltd. Japan. To observe the rotational behavior of the micro objects generated by the photo induced texture changes, glass flakes were sprinkled on the surface of the CLC film followed by the photoirradiation with UV (366 nm, 399 mW cm^{-2}) (Hamamatsu LED controller model c11924−101) and visible light (436 nm, 30 mW cm^{-2}) (super-high-pressure mercury lamp). Microscopic analyses were performed with an OLYMPUS BX-60 polarized optical microscope equipped with a SONY DXC-9503CCD color video camera.

Film thickness was calculated by using equation $\rho = \frac{w}{A*t}$, here ρ is the density of the solution of ZLI-1132 liquid crystal and compound **1**, w is the weight of the solution

spread on the glass surface to prepare film, *A* is the area of the film on glass surface and *t* is the thickness of the film.

Absorption spectra were recorded with an Agilent 8453 spectrophotometer. To set the glass slides with CLC film on the sample holder, I inversed the spectrophotometer. Glass slide was fixed on the sample holder by double sided tape to avoid the any movement of film. Because movement of plate can change the thickness of the film. Before doing the experiment, glass plate was kept in a constant position and condition for overnight to get the homogeneous polygonal fingerprint texture. Photoisomerization process was conducted by using 366 nm and 436 nm light sources and absorbance spectra was recorded.

High pressure liquid chromatography (HPLC) was carried out by Hitachi Elite La Chrome HPLC system with CHIRALPAK IA (DAICEL Chemical Industries Ltd) column using dichloromethane / hexane (30:70) as eluent to determine the *E*/*Z* ratios of azobenzenes in LC or organic solvent medium at isosbestic point of 278 nm.

3.5. References

(1) Vale, R. D.; Milligan, R. A. The Way Things Move: Looking Under the Hood of Molecular Motor Proteins. *Science* **2000**, *288*, 88–95.

(2) Erbas-Cakmak, S.; Leigh, D. A.; McTernan, C. T.; Nussbaumer, A. L. Artificial Molecular Machines. *Chem. Rev.* **2015**, *115*, 10081–10206.

(3) Bissell, R. A.; Córdova, E.; Kaifer, A. E.; Stoddart, J. F. A Chemically and Electrochemically Switchable Molecular Shuttle. *Nature,* **1994**, *369*, 133–137.

(4) Murakami, H.; Kawabuchi, A.; Matsumoto, R.; Ido, T.; Nakashima, N. A Multi-Mode-Driven Molecular Shuttle: Photochemically and Thermally Reactive Azobenzene Rotaxanes. *J. Am. Chem. Soc*. **2005**, *127*, 15891–15899.

(5) Badjic, J. D.; Balzani, V.; Credi, A.; Silvi, S.; Stoddart, J. F. A Molecular Elevator. *Science* **2004**, *303*, 1845–1849.

(6) Ashton, P. R.; Balzani, V.; Kocian, O.; Prodi, L.; Spencer, N.; Stoddart, J. F. A Light-Fueled ″Piston Cylinder″ Molecular-Level Machine. *J. Am. Chem. Soc*. **1998**, *120*, 11190–11191.

(7) Shirai, Y.; Osgood, A. J.; Zhao, Y.; Kelly, K. F.; Tour, J. M. Directional Control in Thermally Driven Single-Molecule Nanocars*. Nano Lett.* **2005**, *5*, 2330–2334.

(8) Muraoka, T.; Kinbara, K.; Aida, T. Mechanical Twisting of a Guest by a Photoresponsive Host. *Nature* **2006**, *440*, 512–515.

(9) Eelkema, R.; Pollard, M. M.; Vicario, J.; Katsonis, N.; Ramon, B. S.; Bastiaansen, C. W. M.; Broer, D. J.; Feringa, B. L. Nano Motor Rotates Microscale Objects. *Nature* **2006**, *440*, 163.

(10) Eelkema, R.; Pollard, M. M.; Katsonis, N.; Vicario, J.; Broer, D. J.; Feringa, B. L. Rotational Reorganization of Doped Cholesteric Liquid Crystalline Films. *J. Am. Chem. Soc.* **2006**, 128, 14397–14407.

(11) Bosco, A.; Jongejan, M. G. M.; Eelkema, R.; Katsonis, N.; Lacaze, E.; Ferrarini, A.; Feringa, B. L. Photoinduced Reorganization of Motor-Doped Chiral Liquid Crystals: Bridging Molecular Isomerization and Texture Rotation. *J. Am. Chem. Soc*. **2008**, *130*, 14615–14624.

(12) Tabe, Y.; Yokoyama, H. Coherent Collective Precession of Molecular Rotors with Chiral Propellers. *Nat. Mater.***2003**, *2*, 806–809.

(13) Orlova, T.; Lancia, F.; Loussert, C.; Iamsaard, S.; Katsonis, N.; Brasselet, E. Revolving Supramolecular Chiral Structures Powered by Light in Nanomotor-Doped Liquid Crystals. *Nat. Nanotechnol.* **2018**, *13*, 304–308.

(14) Yamada, M.; Kondo, M.; Mamiya, J.ichi; Yu, Y.; Kinoshita, M.; Barrett, C. J.; Ikeda, T. Photomobile Polymer Materials: Towards Light-Driven Plastic Motors. *Angew. Chem. Int. Ed.* **2008**, *47*, 4986–4988.

(15) Ma, S.; Li, X.; Huang, S.; Hu, J.; Yu, H. A Light-Activated Polymer Composite Enables On-Demand Photocontrolled Motion: Transportation at the Liquid/Air Interface. *Angew. Chem. Int. Ed.* **2019**, *58*, 2655–2659.

(16) Thomas, R.; Yoshida, Y.; Akasaka, T.; Tamaoki, N. Influence of a Change in Helical Twisting Power of Photoresponsive Chiral Dopants on Rotational Manipulation of Micro-Objects on the Surface of Chiral Nematic Liquid Crystalline Films. *Chem. Eur. J.* **2012**, *18*, 12337–12348.

(17) Kim, Y.; Tamaoki, N. A Photoresponsive Planar Chiral Azobenzene Dopant with High Helical Twisting Power. *J. Mater. Chem. C*. **2014**, *2*, 9258–9264.

(18) Kim, Y.; Tamaoki, N. Asymmetric Dimers of Chiral Azobenzene Dopants Exhibiting Unusual Helical Twisting Power Upon Photoswitching in Cholesteric Liquid Crystals. *ACS Appl. Mater. Interfaces* **2016**, 8, 4918–4926.

(19) Kim, Y.; Frigoli, M; Vanthuyne, N.; Tamaoki, N. Helical Naphthopyran Dopant for Photoresponsive Cholesteric Liquid Crystal. *Chem. Commun*. **2017**, *53*, 200–203.

(20) Bisoyi, H. K.; Li, Q. Light-Driven Liquid Crystalline Materials: From Photo-Induced Phase Transitions and Property Modulations to Applications. *Chem. Rev.* **2016**, *116*, 15089−15166.

(21) Zheng, Z.; Li, Y.; Bisoyi, H. K.; Wang, L.; Bunning, T. J.; Li, Q. Three-Dimensional Control of the Helical Axis of Achiral Nematic Liquid Crystal by Light. *Nature,* **2016**, *531*, 352-356.

(22) Li. Q. *Photoactive Functional Soft Materials: Preparation, Properties, and Applications*, Wiley-VCH, Weinheim, **2019.**

(23) Pace Jr. A. Cholesteric Liquid Crystal-Like Structure of the Cuticle of Plusiotis Gloriosa. S*cience* **1972**, *176*, 678–680.

(24) Kawachi, M.; Kato, K.; Kogure, O. Light Scattering Characteristics in Nematic-Cholesteric Mixtures with Positive Dielectric Anisotropy. *Jpn. J. Appl. Phys*. **1978**, *17*, 1245–1250.

(25) Meister, R.; Hallé, M.; Dumoulin, H.; Pieranski, P. Structure of the Cholesteric Focal Conic Domains at the Free Surface. *Phys. Rev. E* **1996**, *54*, 3771–3782.

(26) Fuh, A. Y. G.; Wu, Z. H.; Cheng, K. T.; Liu, C. K.; Chen, Y. D. Direct Optical Switching of Bistable Cholesteric Textures in Chiral Azobenzene-Doped Liquid Crystals. *Opt. Express*, **2013**, *21*, 21840–21846.

(27) Lai, J. C.; Cheng, W. F.; Liu, C. K.; Cheng, K. T. Optically Switchable Bistable Guest–Host Displays in Chiral-Azobenzene- and Dichroic-Dye-Doped Cholesteric Liquid Crystals. *Dyes Pigments* **2019**, *163*, 641–646.

(28) Thomas, R.; Tamaoki, N. Determination of the Absolute Stereostructure of a Cyclic Azobenzene from the Crystal Structure of the Precursor Containing a Heavy Element. *Beilstein J. Org. Chem.* **2016**, *12,* 2211–2215.

Chapter 4

Conclusion of the Thesis

In this dissertation work, I focused on amplification of novel photoisomerization event of azobenzene based molecules in both artificial and living system to regulate the macroscopic rotational motion and control the cell division, respectively.

For artificial approach, I introduced a molecular system which induced an accumulative unidirectional rotary motion of glass flakes with about 100 μm. The molecular system was a chiral nematic liquid crystal doped with chiral azobenzene derivative which showed different texture change paths upon UV and visible light irradiations inducing "*trans* to *cis*" and "*cis* to *trans*" photoisomerizations, respectively, of the chiral azobenzene dopant. Namely, a polygonal fingerprint texture accumulated the ordered molecular motion of each molecule in macroscopic film and induced the rotation of glass flakes on the film surface during UV irradiation, while scattered domain in focal conic texture induced no rotation of glass flakes emerged during visible light irradiation. As a result, cycles of the alternative irradiation of UV and visible lights afforded many rotations toward a single direction of the glass flakes which can be considered as a continuous conversion of light energy to mechanical work. After 7 complete cycles by UV and visible light irradiations, glass flakes performed around 3000° rotation in one direction. I may compare the effect of this molecular system converting "back and forth" structural change between *trans* and *cis* isomers of the chiral azobenzene to a continuous rotational motion of glass flakes with the crankshaft effect converting a piston-like motion to a rotational motion seen in engines in the real world.

In case of cellular system, I have demonstrated the reversible control of mitosis cell division by transferring the reversible photoisomerization information of azobenzene based molecule. During eukaryotic cell division, the replicated chromosomes are transported from the centrosomes (spindle poles) towards the plus

end of spindle microtubules by the kinesin-like motor protein, centromere-associated protein E (Cenp-E / kinesin 7), which can hydrolyze ATP to produce the mechanical works. While, *trans*-*cis* photoisomerization of azobenzene allowed us to manipulate both activation and inhibition of motor activity of Cenp-E in cells and *in vitro* system. By regulating the Cenp-E activity, it is possible to control the chromosome movements in a reversible mode. Cenp-E was inhibited under *trans* state and induced miscongression of chromosomes and stopped the cell cycle progression, whereas it was not under *cis* state. By using light irradiation, reversible and dynamic control over Cenp-E-driven chromosome movements were addressed in living mitotic cells. This work illustrated the amplification of molecular change under light irradiation to regulate the motor activity of kinesin as well as dynamic cellular processes in living system.

Here, I have highlighted the control of different macroscopic functions by amplifying the photoswitching behavior of azobenzene-based molecules. Both systems can be independently controlled by isomerization signals which allows for tuning the macroscopic response upon light irradiation with two light sources. This work provides interesting insight about the consequences of molecular motions over the macroscopic properties of different systems.

List of Publications

(1) “Molecular Crankshaft Effect Converting Piston-like Molecular Motion to Continuous Rotation of Macro Objects” Mafy, N. N., Kim, Y., Thomas, R., Akasaka, T., Tamaoki, N., *ACS Appl. Mater. Interfaces*, **2019**, *11*, 15097-15102.

(2) “Photochemical Chirality Induction and Inversion in Soft Materials” Kim, Y., Mafy, N. N., Tamaoki. N. *Photoactive Functional Soft Materials: Preparation, Properties and Applications*, Chapter 4, PP: 125-126, Editor: Quan Li, Publisher: Wiley, **2018.**

(3) “Optochemical Motion Control of Chromosomes Driven by Cenp-E During Metaphase” Mafy, N. N.; Matsuo, K.; Hiruma, S.; Uehara, R. Tamaoki, N. (Manuscript under preparation)

Acknowledgements

I would like to express my gratitude and thanks to my supervisor Professor Nobuyuki Tamaoki for his guidance, inspiration, and continuous support throughout the doctoral research.

I am grateful to Dr. Yuna Kim, Dr. Kazuya Matsuo, Dr. Yoshimitsu Sagara for their continuous support to learn synthesis, experimental setup, productive discussions and writing manuscript.

I gratefully acknowledge Dr. Ryota Uehara (Hokkaido University) and his lab members specially Shota Hiruma, for their valuable guidance to learn cell experiments and helpful discussion.

I would like to thank all former and current members of the Professor Tamaoki lab (2016-2019), Dr. Sunil Kumar K. R., Dr. Halley M. M., Dr. A., S., Amrutha, Ms. Hiroko Tayyama, Ms. Emi Kobayashi, Mr. Viswanata H. M., Mr. Ashino F., Ms. Mr. Sampreeth T., Mr. Shariful Haque, Mr. T., Muramatsu, Mr. K., Ueda, Mr. Qi Jiajun, Mr. Lin Runze, Dr. Li Jie and Mr. S. Yutani for their support.

I acknowledge the program organizers of IGP-RPLS. I thank all my friends for helpful and hearty support.

I am financial supported by IGP-RPLS (MEXT) scholarship.

Noushaba Nusrat Mafy